



HAL
open science

Ignition of a confined high explosive under low velocity impact

C. Gruau, D. Picart, R. Belmas, E. Bouton, F. Delmaire-Sizes, J. Sabatier, H. Trumel

► **To cite this version:**

C. Gruau, D. Picart, R. Belmas, E. Bouton, F. Delmaire-Sizes, et al.. Ignition of a confined high explosive under low velocity impact. *International Journal of Impact Engineering*, 2009, 36 (4), pp.537. 10.1016/j.ijimpeng.2008.08.002 . hal-00558628

HAL Id: hal-00558628

<https://hal.science/hal-00558628>

Submitted on 23 Jan 2011

HAL is a multi-disciplinary open access archive for the deposit and dissemination of scientific research documents, whether they are published or not. The documents may come from teaching and research institutions in France or abroad, or from public or private research centers.

L'archive ouverte pluridisciplinaire **HAL**, est destinée au dépôt et à la diffusion de documents scientifiques de niveau recherche, publiés ou non, émanant des établissements d'enseignement et de recherche français ou étrangers, des laboratoires publics ou privés.

Accepted Manuscript

Title: Ignition of a confined high explosive under low velocity impact

Authors: C. Gruau, D. Picart, R. Belmas, E. Bouton, F. Delmaire-Sizes, J. Sabatier, H. Trumel

PII: S0734-743X(08)00218-2

DOI: [10.1016/j.ijimpeng.2008.08.002](https://doi.org/10.1016/j.ijimpeng.2008.08.002)

Reference: IE 1690

To appear in: *International Journal of Impact Engineering*

Received Date: 23 June 2008

Revised Date: 8 August 2008

Accepted Date: 17 August 2008

Please cite this article as: Gruau C, Picart D, Belmas R, Bouton E, Delmaire-Sizes F, Sabatier J, Trumel H. Ignition of a confined high explosive under low velocity impact, *International Journal of Impact Engineering* (2008), doi: [10.1016/j.ijimpeng.2008.08.002](https://doi.org/10.1016/j.ijimpeng.2008.08.002)

This is a PDF file of an unedited manuscript that has been accepted for publication. As a service to our customers we are providing this early version of the manuscript. The manuscript will undergo copyediting, typesetting, and review of the resulting proof before it is published in its final form. Please note that during the production process errors may be discovered which could affect the content, and all legal disclaimers that apply to the journal pertain.





ELSEVIER

**INTERNATIONAL
JOURNAL OF
IMPACT
ENGINEERING**

Ignition of a confined high explosive under low velocity impact

C. Gruau^{a,*}, D. Picart^{a,*}, R. Belmas^a, E. Bouton^a, F. Delmaire-Sizes^a, J. Sabatier^b, H. Trumel^a

^aCEA Le Ripault, BP 16, F-37260 Monts, France

^bUniversité de Bordeaux - CNRS, F-33405 Talence, France

Elsevier use only: Received date here; revised date here; accepted date here

Abstract

In the framework of low velocity impact studies, dedicated to safety analyses of plastic bonded explosives (PBX), we propose a new numerical tool, designed for restituting the ignition of a HMX (high melting point explosive) based composition. Major results are the use of a concrete-like constitutive law for the PBX and an efficient implementation of an ignition criterion. We also put forward two variants of classical Steven tests, which enable us to visualize either a dot ignition or an unusual ring-shaped ignition. It is shown that the calculation tool is able to reconstitute accurately both results. © 2008 Elsevier Science. All rights reserved

Keywords: PBX safety, Steven test, ignition criterion

1. Introduction

High explosive parts confined in pyrotechnic devices can unintentionally ignite, when submitted to impacts, even at low velocities. Ignition can then evolve to more violent and undesired events, such as deflagration or detonation. Prediction of such transitions being hardly tractable, we are focusing our attention on the ignition stage, which is the very first event that must be correctly restituted, in the framework of safety analyses.

The considered high explosive is composed of a poly-dispersed distribution of HMX grains, with a mean diameter of 200 μm , which are mixed with a few percentage of a polymeric binder. An isostatic compaction process is used to reduce the composition porosity at few percentages. Its mechanical response is similar to the behavior exhibited by PBX-9501, another explosive composition.

The low velocity impacts of interest may occur during transport, storage, assembling or disassembling of devices, leading to a great number of accident scenarios. Thus, safety analyses of pyrotechnic structures involve many parameters, like target configuration (shape, materials and boundary conditions) and mechanical loadings (characteristics of the projectile and its movement law), which prevents us from dealing only with experimental techniques. The aim of this paper is to describe a numerical tool designed for the ignition, applied to this kind of accidental configurations.

In order to validate such a numerical tool, an experimental database is needed. The so-called "Steven test", introduced by Chidester and co-workers [1] was modified to simplify the boundary conditions and to limit strain localization [2]. This test is devoted to the determination of a safety threshold (in terms of impact velocity), under which no violent reaction is observed. Figure 1 shows three pictures taken during one of these tests.

* Corresponding author. Tel.: +33-2-47-34-41-73 ; e-mail: cyril.gruau@cea.fr, didier.picart@cea.fr

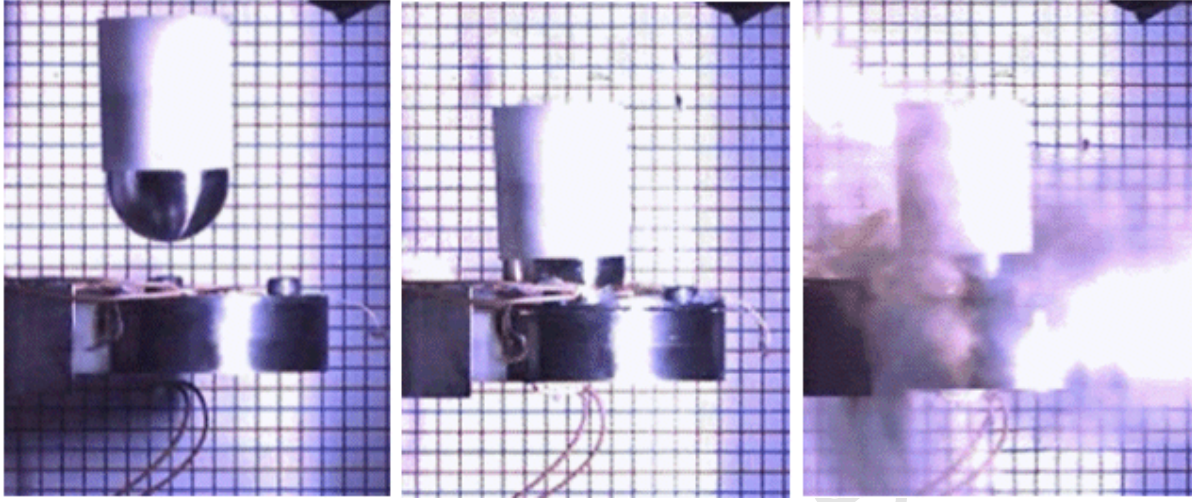


Fig. 1. High speed recording of an impact test (the PBX sample is confined inside the steel target): picture before impact, during impact and at the beginning of reaction (the configuration of the target is given on Figure 15, target 3, projectile velocity = 77 m/s).

Deflagrations and detonations induced by low velocity impacts are not the results of shock-to-detonation transitions, since pressures generated by these impacts are too low. Another mechanism should be invoked; however such a model is beyond the scope of this paper. We actually consider that the material ignites when a sufficient mechanical energy is locally dissipated in the vicinity of defects within the PBX microstructure. Investigations are being made to identify and model the hot spot mechanisms involved in high explosives during ignition. Among all local mechanisms proposed by Field et al. [3], an ignition by low velocity impact is probably caused by frictional heating of preexisting or induced closed micro cracks [4].

Such a frictional heating at the microstructure scale is assumed to result from a macroscopic plastic shear strain under a high level of macroscopic pressure. In other words, frictional heating leads to ignition when the levels and the durations of pressure and plastic shear rate are sufficient. In the literature, several ignition criteria have been proposed, relying on the macroscopic pressure p and on the macroscopic plastic shear strain rate $\dot{\gamma}_{pl}$. Partom [5] used the instantaneous quantity $p \dot{\gamma}_{pl}$, compared with a threshold value of $2.35 \cdot 10^{13} \text{ Pa}\cdot\text{s}^{-1}$. Browning [6] and co-workers [7] employed the time-to-ignition t_{ig} , in a first formula $p^{2/3} \dot{\gamma}_{pl}^{1.27} t_{ig}^{1/4}$, derived from a constant thermal flux assumption. Here, we adopt a criterion based on the work of Browning and Scammon [8], which integrates the history of pressure and plastic shear rate, for varying flux conditions:

$$\frac{1}{c_*} \int_0^{t_{ig}} \left(\frac{t_{ig} - \tau}{t_*} \right)^{-n} \left(\frac{\langle p(\tau) \rangle}{p_*} \right)^{\frac{2n}{3}} \dot{\gamma}_{pl}(\tau) d\tau = 1 \quad (1)$$

where c_* is the threshold value, t_* is a characteristic time, p_* is a characteristic pressure, $\langle p \rangle$ is the positive part of the pressure and the exponent n comes from the HMX decomposition kinetics. When (1) is met, ignition is supposed to occur.

Criterion (1) relies on the computation of the macroscopic pressure and the macroscopic plastic shear rate, inside the high explosive, seen as a continuum. In the history of the Steven test, several material models and several simulation softwares have been used to compute stresses and strains, inside the target. At the beginning, 2D computations were run with a double Jones-Wilkins-Lee equation of state, in conjunction with a reaction model [9]. Other 2D computations [7] were also used with a statistical crack mechanics model [10]. Then, 3D computations were performed, whilst taking a perfect plasticity model for the material [11] and [12].

In fact, a low velocity impact requires a more complex modeling of the PBX behavior, than more violent events (like shocks that induce a pressure dominant state of stress). In the framework of low velocity impacts, the hydrodynamics assumption cannot be made and a tensorial approach of the relationship between stress and strain is adopted, like in impact studies on concrete [13], rock [14] or ceramics [15] structures. Furthermore, the material is very complex itself, involving many difficult issues like: pressure dependence,

coupled with rate dependence, plastic compressibility and anisotropy. Unfortunately, all these ingredients influence the mechanical response of the material under a low velocity impact. Here, we use a concrete-like constitutive law, which involves a hypoelasticity model, a pressure dependent and non-associated plasticity with isotropic hardening. Dilation, dissymmetry between tensile and compression states of stress, altogether with isotropic damage, are taken into account. Some features of the material behavior have not been accounted for yet, like anisotropy due to oriented microcracking or plastic deformation of grains, rate dependent plasticity, a cap yield surface describing compaction at high pressure and a transition between brittle and ductile behavior (strain softening has been taken into account, but in an artificial manner, by a negative hardening evolution).

Abaqus/Explicit was chosen to run computations. This choice is motivated by several reasons. Firstly, we have to deal with continua (thanks to the confinement of the PBX, there is neither pulverization nor fragmentation), whose behaviors exhibit strong nonlinearities under finite strains (but no excessive distortion). So, a Lagrangian finite element method is convenient for our purpose. Secondly, even for low velocity impacts, the strain rate can overcome 10^5 s^{-1} (fast transient dynamics) and the contact between projectile and target can be strongly non linear. So, we focus our attention on an explicit time integration. Thirdly, preliminary tests on low velocity impacts show that Abaqus Explicit exhibits a better energy conservation, a stronger stability and broader functionalities than hydrocodes [16].

When associated to the concrete-like constitutive model and the ignition criterion (1), an Abaqus computation of the target 3 test case (see Figure 15 for a description) indicates that ignition happens at the PBX sample center (Figure 2).

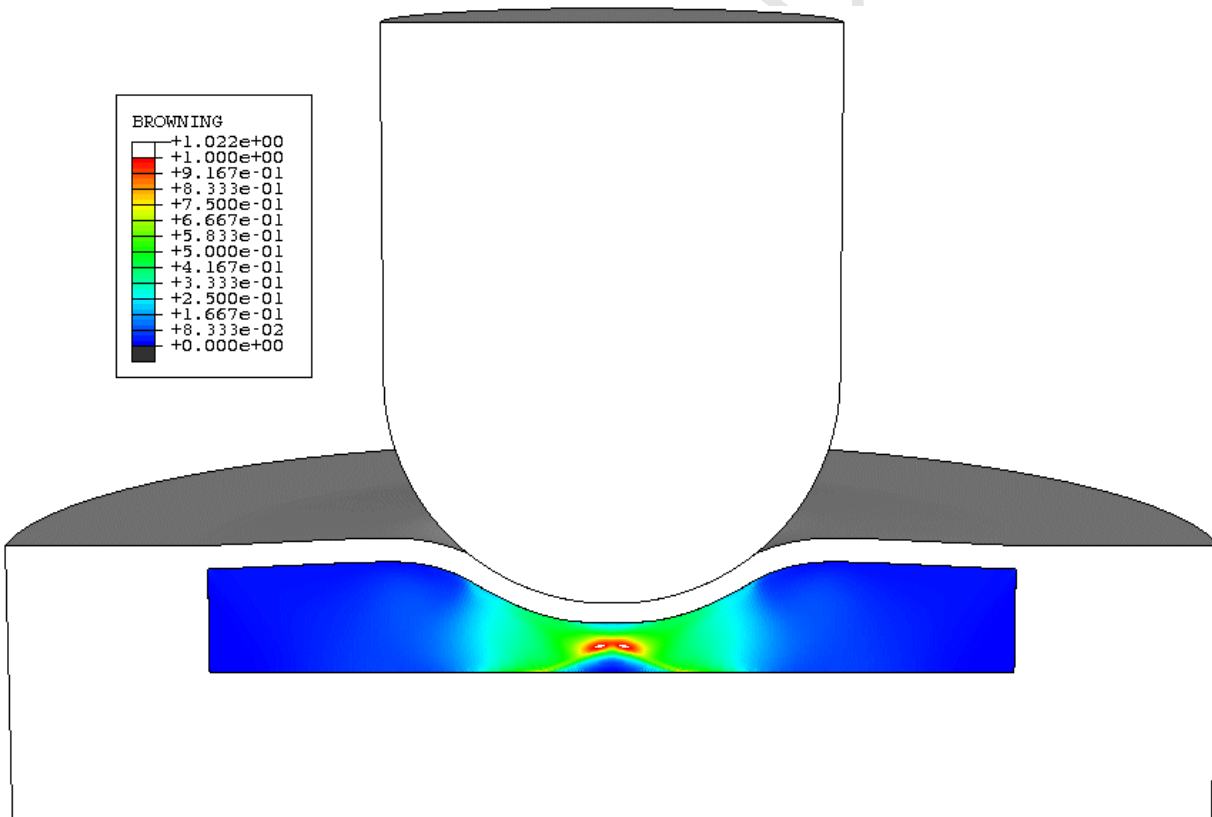


Fig. 2. Computational result of the target 3 test case: the left hand side of equation (1) is denoted by "Browning" in the legend.

The remainder of this paper is devoted to the description of this numerical tool design and is organized in four sections. In section 2, material models are described and the parameter determination is validated against experimental measurements. Building, scaling and implementing of the ignition criterion are detailed in section 3 and appendix 1. Section 4 is devoted to numerical and experimental results obtained for different impact test variants. Finally, in section 5 a summary of the results is drawn and further investigations in progress are emphasized, while a second appendix is dedicated to the HMX decomposition model.

2. Constitutive modeling

In order to take into account many (but not all) influential ingredients on the response of low velocity impacts, the behavior of our PBX is modeled by an elastic-plastic-damage law. This law based on the work of Lubliner and co-workers [17], further improved by Lee and Fenves [18], about concrete materials. This model, called “concrete damaged plasticity” is natively implemented in Abaqus. Here we propose a brief review of the simplified version in use for the PBX. A description of other material models involved in the target and the confinement is also given. Then, confrontations are made between numerical results and experimental measurements.

2.1. PBX modeling

In this model, an isotropic damage is taken into account via a scalar parameter d :

$$\boldsymbol{\sigma} = (1-d) \boldsymbol{\sigma}_{eff} \quad (2)$$

where $\boldsymbol{\sigma}$ is the Cauchy stress tensor and $\boldsymbol{\sigma}_{eff}$ is the effective (undamaged) stress tensor. In our case, the evolution of d depends on the equivalent plastic deformation, but only during tensile loadings:

$$d = r d_t(\bar{\varepsilon}_{pl,t}) \quad \text{with} \quad \bar{\varepsilon}_{pl,t} = \int_0^t r \dot{\varepsilon}_{pl,max} \quad (3)$$

where $\dot{\varepsilon}_{pl,max}$ is the maximal eigenvalue of the plastic strain rate tensor \mathbf{D}_{pl} . The curve $d_t(\bar{\varepsilon}_{pl,t})$ is given by an experimental characterization.

In expressions (3), the scalar variable r takes a continuous value between 0 and 1, quantifying the proportion of strictly positive eigenvalues of $\boldsymbol{\sigma}$, via $r = \frac{\langle \sigma_1 \rangle + \langle \sigma_2 \rangle + \langle \sigma_3 \rangle}{|\sigma_1| + |\sigma_2| + |\sigma_3|}$ (classical notations are adopted: $\langle \rangle$ stands for positive part and $|\cdot|$ for absolute value). Its use in the computation of d enables stiffness recovery in compression (for such stress states, r decreases and $(1-d)$ tends to 1).

Then, the elastic strain is assumed to be small enough for the additive decomposition to be adopted. Elastoplasticity is written in terms of the hypoelastic Jaumann stress rate:

$$\overset{\nabla}{\boldsymbol{\sigma}}_{eff} = K : (\mathbf{D} - \mathbf{D}_{pl}) \quad (4)$$

where K is the Hookean (isotropic) elastic stiffness tensor and \mathbf{D} is the total strain rate tensor.

The yield function f is an extension of the linear Drucker-Prager criterion, using a friction angle φ , as follows:

$$f = q_{eff} - p_{eff} \tan \varphi - \left(1 + \frac{\tan \varphi}{3}\right) \langle \sigma_{eff,max} \rangle + \left(1 - \frac{\tan \varphi}{3}\right) \langle \sigma_{eff,max} \rangle \frac{\sigma_{Y,c}}{\sigma_{Y,t}} - \left(1 - \frac{\tan \varphi}{3}\right) \sigma_{Y,c} \quad (5)$$

where $p_{eff} = -\frac{1}{3} \text{Trace}(\boldsymbol{\sigma}_{eff})$ is the effective pressure and $q_{eff} = \sqrt{\frac{3}{2} (\boldsymbol{\sigma}_{eff} + p_{eff} \mathbf{I}) : (\boldsymbol{\sigma}_{eff} + p_{eff} \mathbf{I})}$ is the effective von Mises stress (\mathbf{I} being the identity matrix). The friction angle is determined from several triaxial compression tests (quasi-static), performed at different confining pressures. A value of 20° agrees well with pressures between 40 MPa and 230 MPa (Figure 3). At zero pressure, an initial yield stress of 5 MPa is considered. Strength loss is reached at a tensile pressure of about -13 MPa.

A major difference between (5) and the linear Drucker-Prager criterion is the influence of the third invariant, via the maximal eigenvalue denoted by $\sigma_{eff,max}$. Besides, criterion (5) uses two yield stresses, one in compression $\sigma_{Y,c}$ and one in tension $\sigma_{Y,t}$, which enables us to deal with the great dissymmetry between compression behavior (rather ductile) and tensile behavior (brittle).

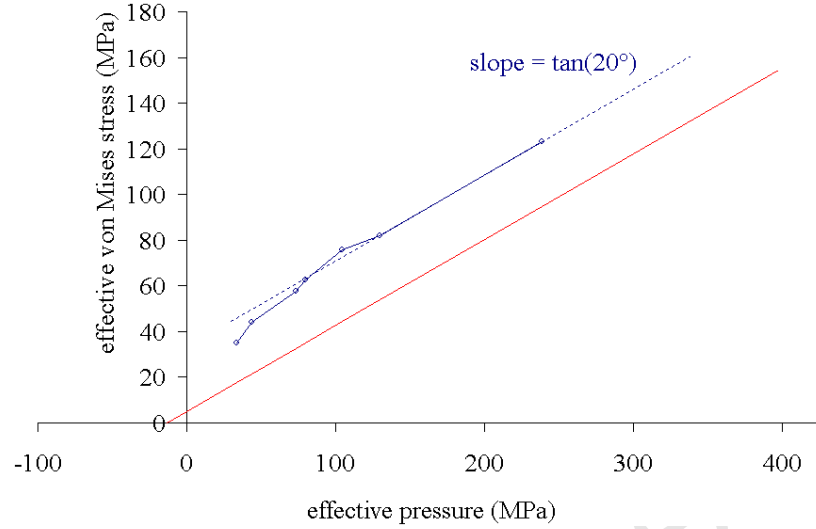


Fig. 3. Friction angle determination: ultimate yield stresses obtained with triaxial compression tests (in blue) and the considered initial yield function (in red) are plotted against the effective pressure.

Strain softening in tension is given by $\sigma_{Y,t}(\bar{\epsilon}_{pl,t})$, while strain hardening in compression is given by:

$$\sigma_{Y,c}(\bar{\epsilon}_{pl,c}) \quad \text{with} \quad \bar{\epsilon}_{pl,c} = \int_0^t (r-1) \dot{\epsilon}_{pl,\min} \quad (6)$$

where $\dot{\epsilon}_{pl,\min}$ is the minimal eigenvalue of \mathbf{D}_{pl} . Both strain-stress curves are plotted on Figure 4.

Unfortunately, our model for compression cannot take the (experimentally observed) brittle-to-ductile transition into account. So, two assumptions are made. Firstly, strain hardening is identified at a 200 MPa confining pressure (which is the order of magnitude in an impact test). Secondly, a strain softening effect is introduced after a compressive plastic strain of 20 %, with a slope of -53 MPa .

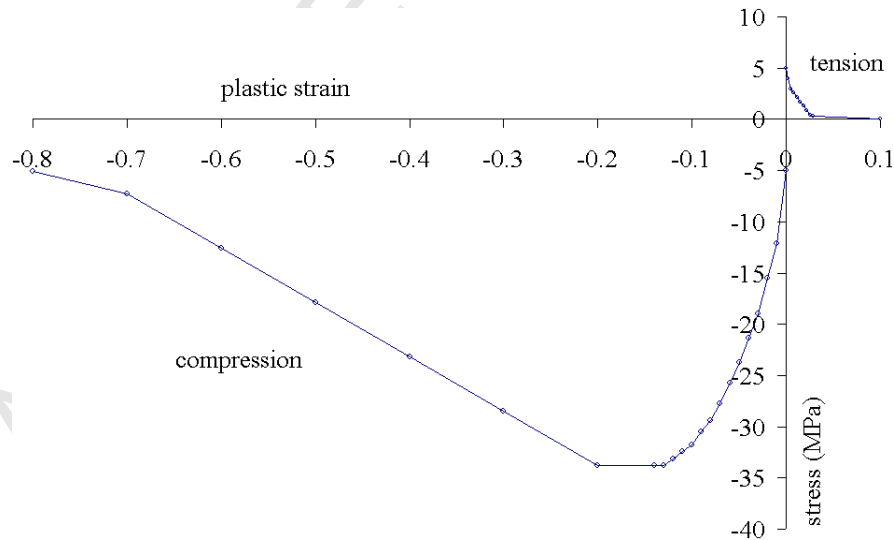


Fig. 4. Isotropic strain hardening curve in tension and compression (unconfined).

A non-associated plastic flow is considered via the hyperbolic Drucker-Prager plastic potential, using a dilation angle ψ :

$$g = \sqrt{q_{eff}^2 + (e \sigma_{y,t}(0) \tan \psi)^2} - p_{eff} \tan \psi \quad (7)$$

where e is the eccentricity and $\sigma_{y,t}(0)$ is the initial value of the yield stress in tension. The dilation angle is determined so as to reproduce the transversal response, observed on the triaxial compression tests. Figure 5 shows both longitudinal and transversal curves for different confining pressures (from 25 MPa to 800 MPa). A low value of 1° leads to a good agreement between the computed transversal curves and the experimental ones, at finite strain.

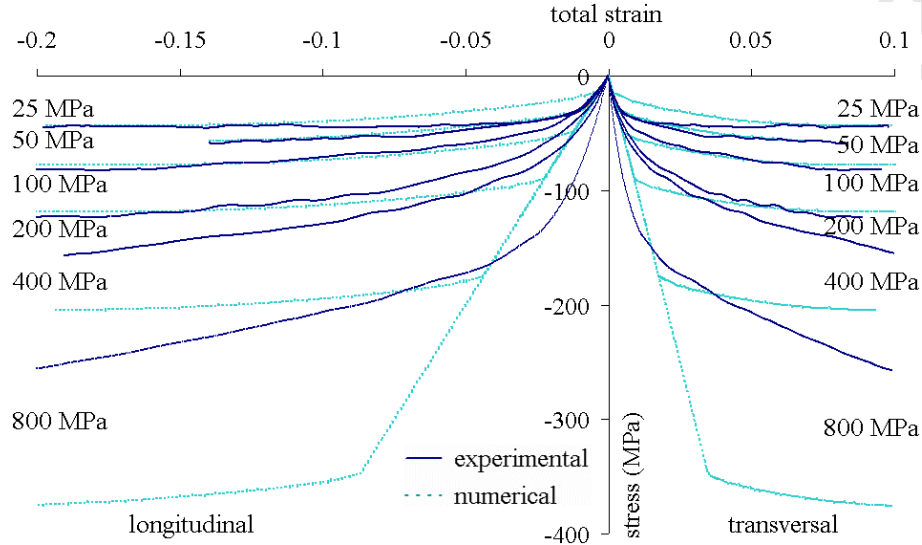


Fig. 5. Longitudinal and transversal behaviors for different confining pressures. Comparisons between experimental results and numerical approximation.

2.2. Materials parameters

The material parameters used for the PBX are summarized in Table 1. The dilation angle is lower than the friction angle, ensuring that plastic dissipation is positive.

Table 1. Material parameters for the PBX.

parameters	value
density	1800 kg.m ⁻³
Young modulus	4 GPa
Poisson's ratio	0.4
friction angle	20°
dilation angle	1°
eccentricity	0.1
initial yield stress	5 MPa
compressive strain softening slope	-53 MPa

Other materials are involved in impact tests. The projectile is made of stainless steel and the confinement can be composed of: stainless steel, Plexiglas (PMMA), Teflon (PTFE) and transparent glass (Figures 15 and 16). Glass and Plexiglas are not supposed to fail during the tests; an isotropic elastic model is adopted. Steel and Teflon are ductile, but they are also not supposed to fracture during the tests; an elastoplastic model is used, with a perfect plasticity for steel (a Johnson-Cook failed to give more accurate results) and with linear strain hardening up to 20 MPa for Teflon (Table 2).

Table 2. Parameters for other materials.

parameters	steel	Plexiglas	glass	Teflon

density	7850 kg.m ⁻³	1190 kg.m ⁻³	2510 kg.m ⁻³	2200 kg.m ⁻³
Young modulus	210 GPa	3.3 GPa	81 GPa	0.46 GPa
Poisson's ratio	0.3	0.34	0.28	0.46
initial yield stress	400 MPa			9 MPa
ultimate yield stress	400 MPa			20 MPa

Friction between PBX and steel is modeled by a constant friction coefficient (without threshold). Other contact interactions (especially between PBX and glass or Plexiglas) are assumed to be frictionless.

2.3. Comparisons between experiments and numerical results

Confrontation between experimental and numerical results, obtained with the aforementioned models and parameters, is performed on impact tests, on instrumented targets. Like in [7], [9] and [12], instrumentation consists in strain and pressure gauges. We also use post-mortem observations made on soaked targets, especially to quantify the permanent strain and fracture.

In what concerns the test case of Figures 1 and 2, the target contains a 100 mm diameter and 13 mm thick PBX sample, within a 150 mm diameter and 35 mm thick cylindrical steel confinement. A hemispherical steel projectile of 1.2 kg is launched at 77 m/s. The impacted target was equipped with a strain gauge placed in the center of the confinement rear face.

During the first 100 μ s (Figure 6), numerical and experimental strains increase in the same way (except a slight delay for the numerical one). Then, the numerical curve shows a plateau around 0.25 %, which is nearly the value of the first experimental peak. Unlike the experimental result, the numerical one does not oscillate, except after 300 μ s, but with an opposite phase.

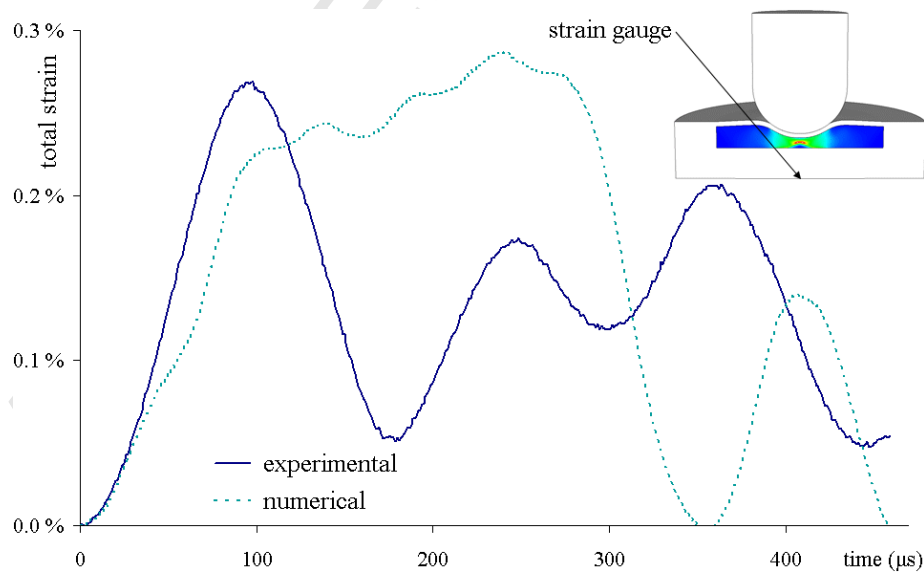


Fig. 6. Comparison between strain evolutions.

A central pressure gauge had also been placed between the front confinement and the explosive. Numerical results show a first plateau above 100 MPa, while the experimental gauge records two peaks under 100 MPa (Figure 7). Then, pressure rises in both cases, but the third experimental peak at 60 μ s is not reproduced numerically. The largest calculated value is under 500 MPa and is attained before 270 μ s, although the largest experimental value is about 550 MPa and is attained at 180 μ s. The experimental pressure decrease after 200 μ s is quite well restituted (though delayed), up to 300 μ s where a violent reaction makes the experimental gauge signal increase suddenly.

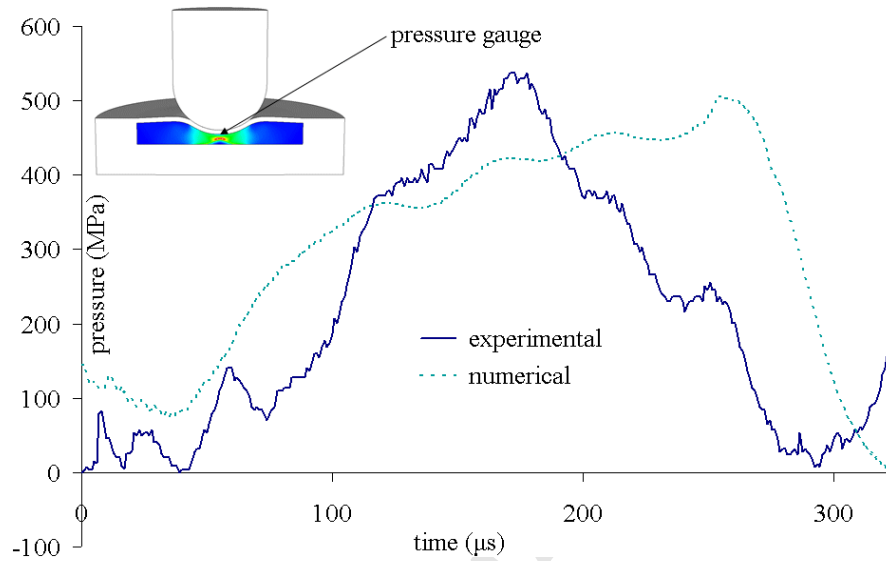


Fig. 7. Comparison between pressure evolutions.

Another target, corresponding to a non reactive test case, was soaked, sliced and photographed (target 2, hemispherical projectile, according to Figure 15). Here, we use this information in order to measure the permanent strain and the fracture underwent by the PBX sample (Figure 8). Consequent profile and thickness sizes along the radius agree well between computations and measures.

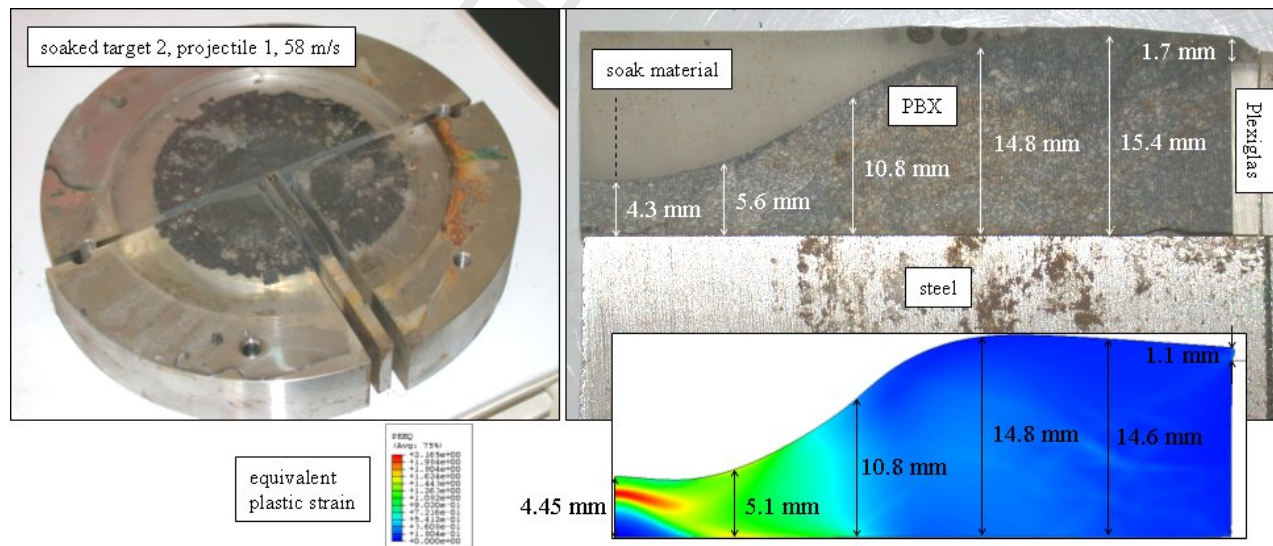


Fig. 8. Comparison between observed and calculated post-mortem sample (target 2, hemispherical projectile, following the Figure 15 numbering)

This confrontation between numerical and experimental results does not perfectly validate the current state of the material modeling and deserves further investigations on rheological characterization. However, agreement between the curves of Figures 6 and 7 is not so bad until ignition (before 100 μ s and under a pressure of 300 MPa), which does not prevent us from performing relevant safety studies.

3. Ignition criterion

Even in a nearly adiabatic framework (since the PBX conductivity is low and since the mechanical stimulus is shorter than 1 ms), the macroscopic temperature rise, due to plastic dissipation, does not exceed 40 K (except at contact between PBX and confinement, where a plastic strain localization occurs). Thus, a PBX thermal ignition due to a low velocity impact cannot be explained at the macroscopic scale, but rather at the microscopic one. As stated in the introduction, the heating mechanism privileged in our modeling is a local friction between HMX grains.

The Browning & Scammon ignition criterion [8], described in this section (without innovation, except in what concerns its computation), is based on the dissipation generated by friction between HMX grains. Macroscopic pressure and plastic shear rate are transferred to a simple microstructure representation. Then, the criterion is used to compute whether the local heating, due to these quantities, is sufficient for the material to ignite. This criterion can take into account ignition through localization at adiabatic shear bands, like in [19], since frictional heating between grains is compatible with shear banding. In fact, the Browning & Scammon criterion can take into account the high level of plastic shear strain inside these bands, whose size is comparable with the coarse grain size.

3.1. Criterion building

Although a wide range of grain sizes and the presence of a polymeric binder should be taken into account for our material, the microstructure is assumed to be a 3D regular sphere packing of identical HMX grains (Figure 9). A sample is subjected to a compressive macroscopic pressure $\langle p(t) \rangle$ and a macroscopic plastic shear rate $\dot{\gamma}_{pl}(t)$. Only the plastic part of shear rate is considered, since micro-surfaces are not supposed to slide during elastic loadings and unloadings.

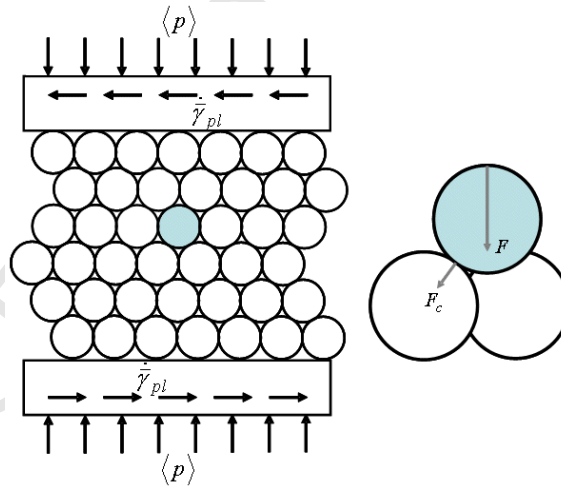


Fig. 9. Schematics of the microstructure and notations.

Positive pressure $\langle p(t) \rangle$ is transferred at the grain scale into a contact force $F_c(t)$, applying between two adjacent grains, which is proportional to $\langle p(t) \rangle$. Thus, there exists a constant area a_1 , such that:

$$F_c(t) = a_1 \langle p(t) \rangle \quad (8)$$

Considering a Hertzian contact between two adjacent grains (Figure 10), the contact surface radius $R_c(t)$ is proportional to $F_c^{1/3}(t)$. So, there exists a constant a_2 ($\text{m.Pa}^{-1/3}$), such that:

$$R_c(t) = a_2 \langle p(t) \rangle^{1/3} \quad (9)$$

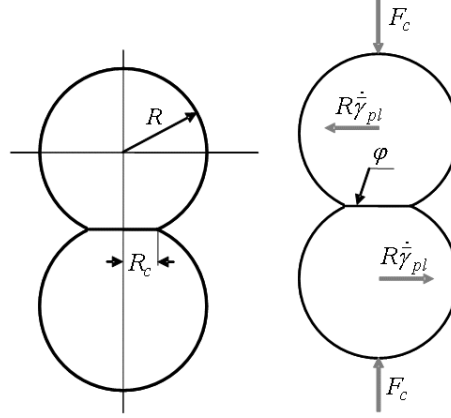


Fig. 10. Hertzian contact and frictional dissipation.

Furthermore, the mean contact pressure $p_c(t)$ on the contact surface is proportional to $\frac{F_c(t)}{R_c^2(t)}$. A constant $a_3 = a_1 a_2^{-2}$ ($\text{Pa}^{2/3}$) can be found, such that:

$$p_c(t) = a_3 \langle p(t) \rangle^{1/3} \quad (10)$$

Then, the average heat flux $\varphi(t)$, induced by frictional dissipation, is assumed to be proportional to $p_c(t) \dot{\gamma}_{pl}(t)$. So, a constant a_4 ($\text{m.Pa}^{2/3}$) can be defined such that:

$$\varphi(t) = a_4 \langle p(t) \rangle^{1/3} \dot{\gamma}_{pl}(t) \quad (11)$$

Now, an ignition criterion can be expressed as follows:

$$\int_0^{t_{ig}} K \left(\frac{t_{ig} - \tau}{R_c^2(\tau)} \right) \varphi(\tau) \frac{d\tau}{R_c(\tau)} = 1 \quad (12)$$

where K is a kernel that depends on the HMX chemical decomposition kinetics.

To determine the kernel K , we consider a stationary case, namely $\varphi(t) = \bar{\varphi}$ and $R_c(t) = \bar{R}_c$. In this case, ignition criterion (12) can be expressed as follows:

$$\int_0^{t_{ig}} K \left(\frac{t_{ig} - \tau}{\bar{R}_c^2} \right) \frac{d\tau}{\bar{R}_c} = \frac{1}{\bar{\varphi} \bar{R}_c} \quad (13)$$

In this context, Browning and Scammon [8] proved that a power law relationship can be established between $\bar{\varphi} \bar{R}_c$ and $\frac{t_{ig}}{\bar{R}_c^2}$,

by considering a thermal decomposition of HMX, based on the global multistep chemical kinetic model proposed by Tarver [20] and [21] (see appendix 2). This power law introduces a new constant a_5 ($\text{J.m}^{-3} \cdot (\text{m}^2 \cdot \text{s}^{-1})^n$):

$$\bar{\varphi} \bar{R}_c = a_5 \left(\frac{t_{ig}}{\bar{R}_c^2} \right)^{n-1} \quad (14)$$

Here, we will take a value of 0.447 for n (appendix 2).

Combining (13) and (14), we obtain the following equation for K :

$$\int_0^{t_{ig}} K \left(\frac{t_{ig} - \tau}{R_c^2} \right) \frac{d\tau}{R_c^2} = \frac{1}{a_5} \left(\frac{t_{ig}}{R_c^2} \right)^{1-n} \quad (15)$$

which solution is $K(x) = a_6 x^{-n}$, where $a_6 = \frac{1-n}{a_5}$.

Thus, (12) can be rewritten as:

$$\int_0^{t_{ig}} (t_{ig} - \tau)^{-n} R_c^{2n-1}(\tau) \varphi(\tau) d\tau = \frac{1}{a_6} \quad (16)$$

and combining with (9) and (11), yields to:

$$\int_0^{t_{ig}} (t_{ig} - \tau)^{-n} \langle p(\tau) \rangle^{2n/3} \dot{\gamma}_{pl}(\tau) d\tau = a_7 \quad (17)$$

with a constant threshold a_7 (in $s^{-n} \cdot Pa^{2n/3}$). In order to remove the units of quantities elevated to a non-integer power, we introduce a characteristic time t_* and a characteristic pressure p_* . Then, with a threshold value c_* (dimensionless), (17) can be recast into the following dimensionless form:

$$\frac{1}{c_*} \int_0^{t_{ig}} \left(\frac{t_{ig} - \tau}{t_*} \right)^{-n} \left(\frac{\langle p(\tau) \rangle}{p_*} \right)^{\frac{2n}{3}} \dot{\gamma}_{pl}(\tau) d\tau = 1$$

An efficient and accurate computation relies on a Prony series approximation (appendix 1). The relative error of the numerical scheme (23)-(24) is quantified in the following section, after a needful signal filtering.

3.2. Threshold value

The computation of $\dot{\gamma}_{pl}(\tau)$ by an explicit solver leads usually to a very noisy signal $\tilde{f}(\tau) = \langle p(\tau) \rangle^{2n/3} \dot{\gamma}_{pl}(\tau)$. With such a raw signal, integral (19) would inherit much numerical noise, which would prevent us from determining a discriminating threshold value for the ignition criterion.

Hence, we apply a low pass filter to $\tilde{f}(\tau)$, so as to obtain a filtered signal $f(\tau)$, used in the criterion computation (previous section). A third order Bessel filter was chosen, because of a sufficiently regular gain and a predictable phase shift (which is nearly the cutting frequency inverse).

This filter relies on the following scheme:

$$\begin{cases} \ddot{f}(t) = (1 - 6 \omega_c \delta t) \ddot{f}(t - \delta t) - 15 \omega_c^2 \delta t \dot{f}(t - \delta t) + 15 \omega_c^3 \delta t (\tilde{f}(t) - f(t - \delta t)) \\ \dot{f}(t) = \dot{f}(t - \delta t) + \frac{\delta t}{2} (\ddot{f}(t) + \ddot{f}(t - \delta t)) \\ f(t) = f(t - \delta t) + \frac{\delta t}{2} (\dot{f}(t) + \dot{f}(t - \delta t)) \end{cases} \quad (18)$$

where δt is the time increment and ω_c is the cutting frequency (at $t = 0$ we consider $f = 0$, $\dot{f} = 0$ and $\ddot{f} = 0$).

Empirically, a cutting frequency of 200 kHz leads to a correct filtering of the signal (Figure 11), with a reasonable phase shift of nearly 5 μs on the criterion evolution (Figure 12).

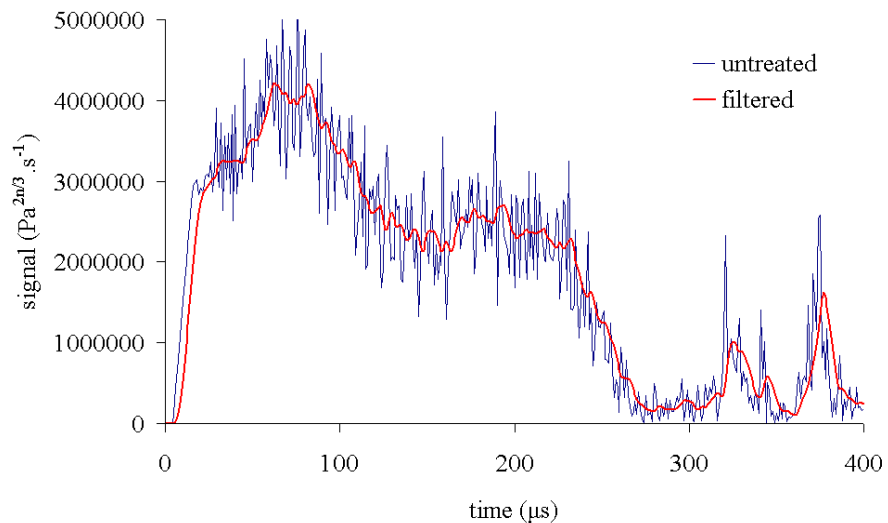


Fig. 11. Filtering of the signal at an integration point: the noise is highly reduced.

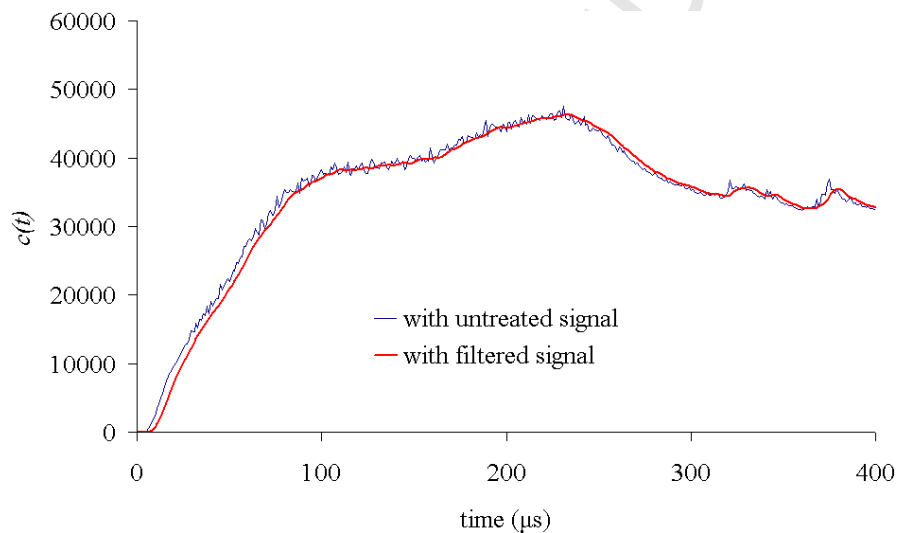


Fig. 12. Consequence on the criterion evolution, at the same integration point: the noise is highly reduced, but an offset of nearly 5 μs is introduced.

This filter works well in smoothing the signal field (Figure 13). These time and spatial noise reductions facilitate the determination of the ignition time and location.

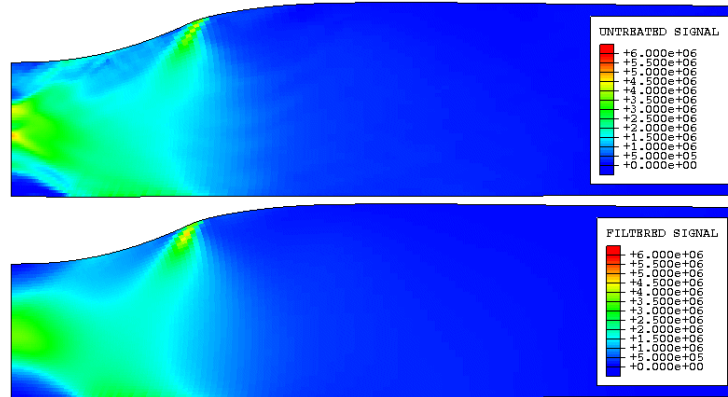


Fig. 13. Smoothing of the signal field at an intermediate time step: spatial noise is reduced.

Once applied to the filtered signal, the approximate criterion agrees well with the exact one (Figure 14). Except at early times, where a high accuracy is not required, the relative error decreases rapidly beneath 5%. Thus, the scheme (23)-(24) shows a good behavior.

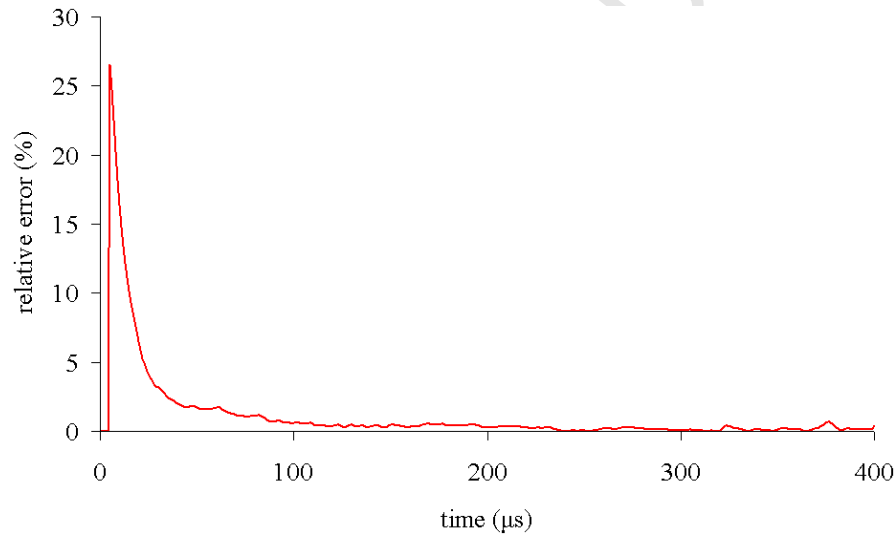


Fig. 14. Evolution of relative error between exact and approximated criterion at the same integration point.

Now, the quantity $c(t)$ can be computed at each integration point and if its value is greater than c_* , ignition occurs. However, the threshold value c_* remains to be calibrated. For the sake of simplicity, we consider a characteristic time t_* of 1 s and a characteristic pressure p_* of 1 Pa. Then, an experimental database, involving several reactive and non reactive tests, is used to determine a lower bound and an upper bound for c_* . This database relies on four configurations, with different confinements and different projectiles (Figure 15).

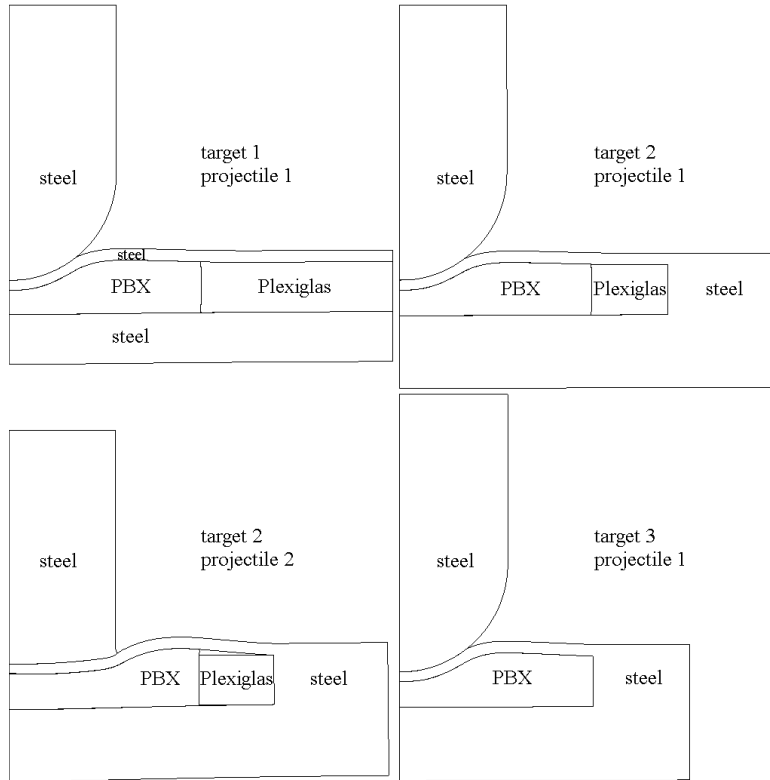


Fig. 15. Four axi-symmetrical impact test configurations (deformed geometries at $100 \mu\text{s}$) are used for determining an ignition threshold.

For a non reactive case, the maximum value of $c(t)$ (in space and time) is a lower bound for the threshold. Meanwhile, for a reactive case, the maximum value of $c(t)$ (in space and time) is an upper bound for the threshold (Table 3). Finally, a value of $4.868 \cdot 10^4$ for c_* is compatible, according to the upper and lower bounds obtained with our four configurations.

Table 3. Upper and lower bounds for the threshold value.

configurations	highest non reactive velocities	lowest reactive velocities	threshold lower bounds	threshold upper bounds
target 1 projectile 1	77 m/s	84 m/s	$4.281 \cdot 10^4$	$4.925 \cdot 10^4$
target 2 projectile 1	62 m/s	76 m/s	$4.867 \cdot 10^4$	$8.693 \cdot 10^4$
target 2 projectile 2	76 m/s	81 m/s	$4.302 \cdot 10^4$	$4.871 \cdot 10^4$
target 3 projectile 1	61 m/s	77 m/s	$4.066 \cdot 10^4$	$7.523 \cdot 10^4$

Figures 2, 18 and 19 display the scalar field $\frac{1}{c_*} c(t)$, which is greater than 1 when ignition occurs.

4. Confrontations between simulations and experiments

Previous impact test configurations were dedicated to a velocity threshold determination. However, their design prevents us from determining the ignition location and time of reactive cases. So, the computed ignition time of $98 \mu\text{s}$ for the test case

of Figure 2, with a small ring-shaped (or a cap-shaped) ignition zone, cannot be validated experimentally, with the target 3 configuration. That is the reason why two new configurations with a transparent visualization window were designed (Figure 16), allowing fast video recording.

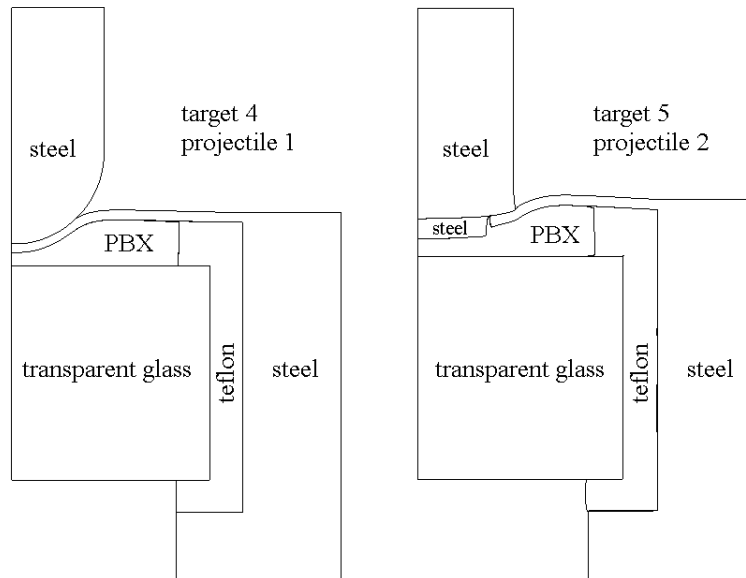


Fig. 16. Two new axi-symmetrical impact test configurations (deformed geometries at $100 \mu\text{s}$) are used to determine the ignition time and location.

The first configuration, with the round nosed projectile, leads to the observation of a punctual ignition (next section). The second configuration, with a nearly flat projectile and a puncher, was designed so as to obtain a ring-shaped ignition area (section 4.2). Experiments and simulations were performed with both configurations, so as to evaluate the capabilities of the numerical tool.

4.1. Impact test with rear visualization

The former configuration involves a hemispherical nosed projectile, launched at 103 m/s . The first lightening event is recorded between $50 \mu\text{s}$ and $60 \mu\text{s}$ (Figure 17). This experimental lightening event is due to local ignition, which is roughly located at PBX center and near the PBX rear face. The timestamp of $60 \mu\text{s}$ is considered as an upper bound of the computed ignition time, since the transition to lightening is not modeled. $60 \mu\text{s}$ is a classical time to ignition for low velocity impacts (contrary to shock ignition in 1 microsecond), even shorter than already observed time to ignition in references [1], [7], [9] and [11].

The computation of this test case indicates an ignition at $53 \mu\text{s}$ (Figure 18), which is coherent with the $60 \mu\text{s}$ experimental upper bound (the filter delay of $5 \mu\text{s}$ being taken into account). Furthermore, the computed ignition zone is punctual and located at the center of the PBX rear face. In fact, no integration point lies exactly on the axis and, even in the vicinity of the axis, plastic shear strain is not negligible. Ignition occurs near the axis because the pressure level is very high at this place, with a strictly positive plastic shear strain. At the projectile radius, shear strain is higher, but the pressure level is not high enough to lead to ignition.

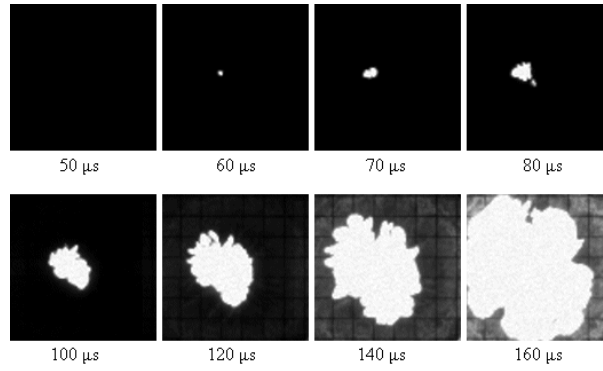


Fig. 17. High speed recording of the rear face (target 4 test case).

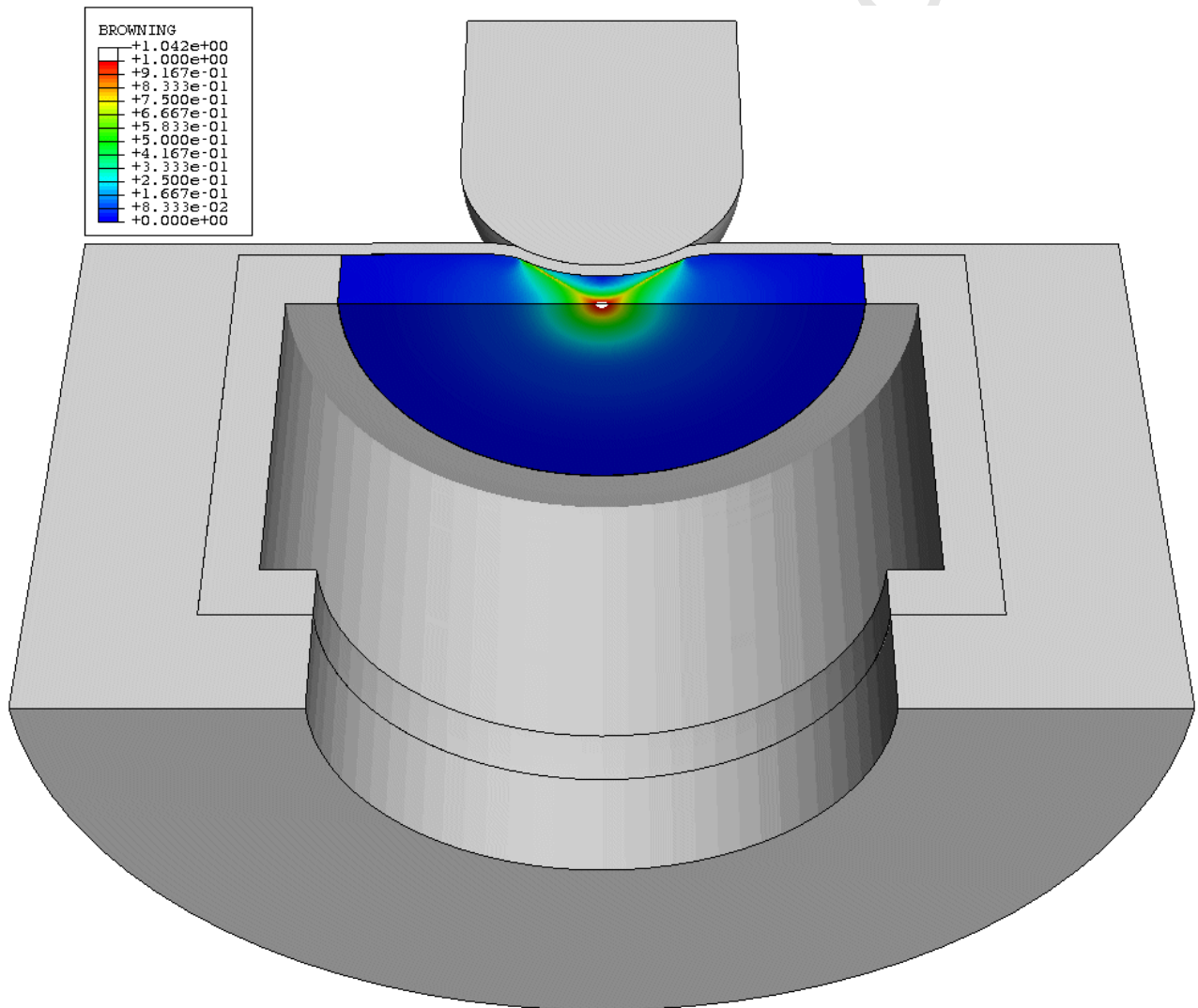


Fig. 18. Computational result at 53 μs of the target 4 test case.

4.2. Impact test with a penetrating part

As for the classical tests, the previous configuration is a non penetrating impact, leading to a single dot ignition. Actually, safety analyses of pyrotechnic structures may involve scenarios with penetrating projectiles. We thus derived another configuration, with a hole pierced in the front confinement, in order to insert a cylindrical puncher (Figure 16 on the right). This puncher penetrates the PBX sample, when impacted by a flat nosed projectile, launched at 110 m/s. In this case, shear strain is enhanced and the pressure level remains high.

The numerical results show that ignition takes place before $55 \mu\text{s}$ (Figure 19), not only around the puncher corner (where the stimulus is quite severe, excluding an artifact), but also along a ring-shaped zone on the PBX rear face. The ring diameter is 12.6 mm.

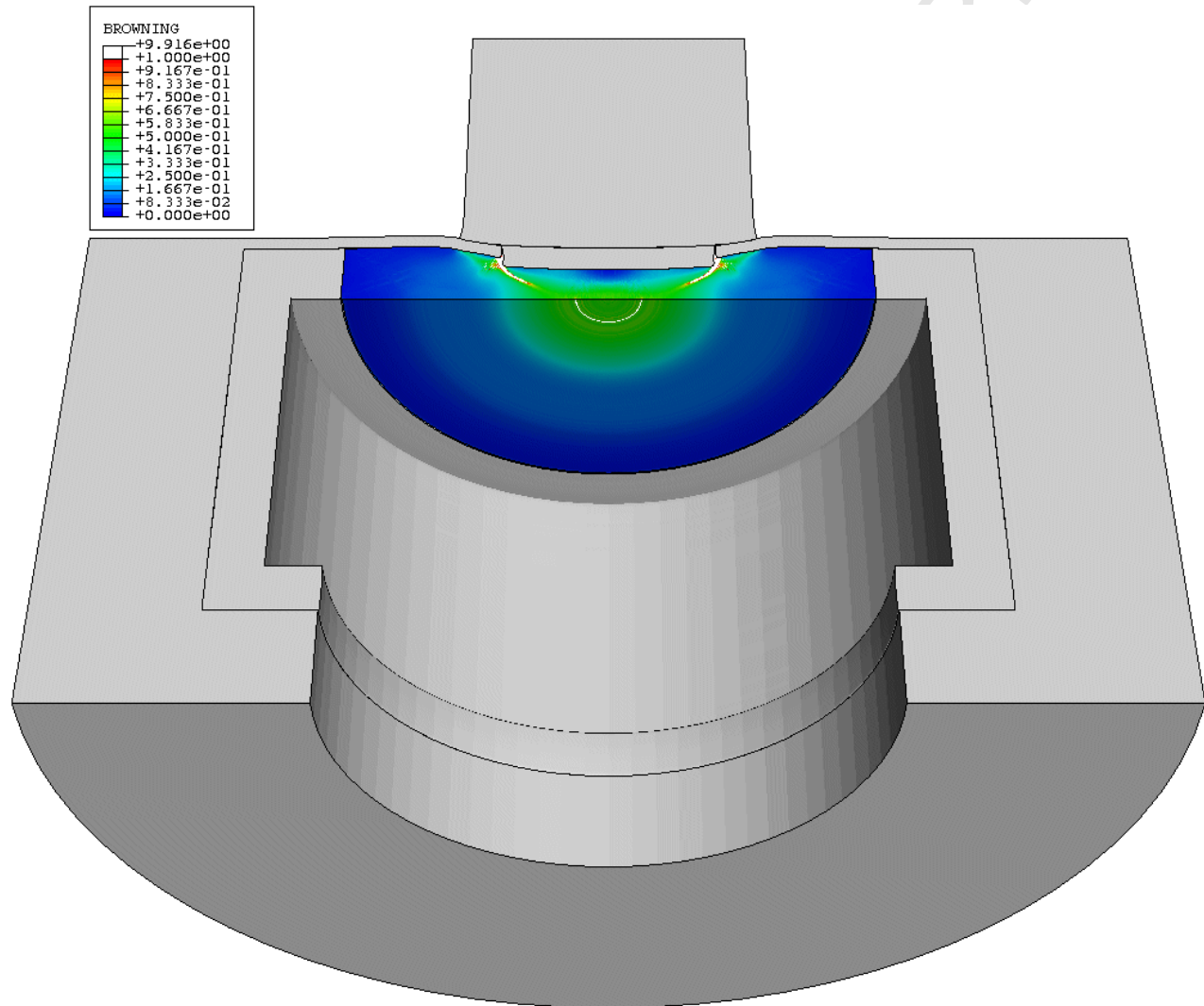


Fig. 19. Computational result at $55 \mu\text{s}$ of the new penetrating reactive test (target 5).

The corresponding experimental test was then performed, with a fast video recording (Figure 20). The very first lightening event appears between $53 \mu\text{s}$ and $60 \mu\text{s}$. Again, the ignition time is correctly restituted. This experimental result validates the computed ring-shaped ignition on the PBX rear face. However, the experimental diameter is evaluated to be of nearly 25 mm, which is twice as the computed diameter.

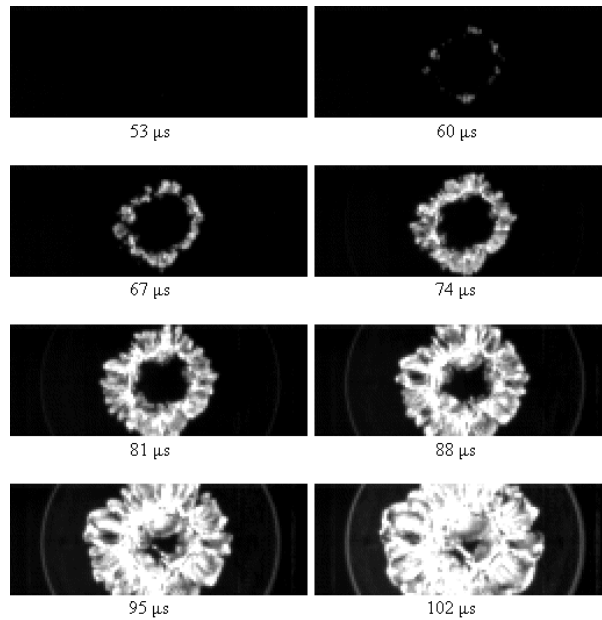


Fig. 20. High speed recording of the target 5 test case.

Furthermore, the fact that numerical simulation raises two separate ignition zones can be explained by the lack of a characterization about compressive strain softening in the material model. Without any experimental measurement, strain localization may not be well reproduced, so that a shear band connects both ignition zones.

5. Conclusion

In this paper, we propose two extensions of the classical Steven impact test, in order to validate a numerical tool for ignition under a low velocity impact. Major improvements are the ability to visualize the ignition location, the ignition time and the ability to generate shear induced ignition via a puncher.

This numerical tool relies on an existing ignition model and its threshold value. This criterion integrates the macroscopic pressure and the macroscopic plastic shear strain rate, using an accurate and efficient approximation by Prony series. Computation of these macroscopic quantities involves a concrete-like constitutive model for the PBX material, with pressure-dependent plasticity and dilation. Triaxial compressive tests, at different confining pressures, are used to determine the friction and the dilation angles.

In this framework, instrumented targets are used to compare the calculated and the measured strain and pressure evolutions. Meanwhile, post-mortem analyses make it possible to correlate the final target dents. Impact tests are also used to calibrate the ignition model threshold value and to compare computed ignition time and location to measurements. This confrontation is quite fair, even if remaining discrepancies are still observed and should deserve further work on the constitutive models.

The numerical tool is not a definitive one, great progresses remains to achieve. Work in progress is focusing on material characterization and modeling, as an extension of [25] and [26], which involves difficulties to attain both high pressures and high strain rates, in finite strain. Furthermore, our PBX is also modeled at the microscopic scale, so as to improve the estimation of the energy dissipation generated by friction of closed microcracks, as initiated in [27] and [28]. Developments about shear banding (localization limiter) and macroscopic fracture (discontinuity tracking) are also under investigation.

Appendix 1: Ignition criterion computing

In order to determine whether ignition occurs or not in the calculation, the following quantity has to be computed:

$$c(t) = \int_0^t (t-\tau)^{-n} f(\tau) d\tau \quad (19)$$

where $f(\tau)$ is a signal function to be integrated with the kernel $(t-\tau)^{-n}$. Unfortunately, since n is not an integer, neither a simplifying Laplace transform, nor a Taylor development can lead to a simple incremental scheme. Furthermore, computing $c(t)$ at each time step of the simulation, would involve the storage of all the signal history and an expensive numerical integration, from the initial time. A discretization of kernel $(t-\tau)^{-n}$ could reduce the computational cost, but not the storage.

That is the reason why, following the work of [23] and [24], kernel $(t-\tau)^{-n}$ is replaced by a Prony series, so as to reduce both computational cost and storage. This Prony series approximation consists in considering:

$$\int_0^t (t-\tau)^{-n} f(\tau) d\tau \cong C \left(A_0 f(t) + \sum_{k=1}^N A_k \omega_k \int_0^t \exp(-\omega_k(t-\tau)) f(\tau) d\tau \right) \quad (20)$$

where C is a constant, A_k and ω_k are suitable amplitudes and frequencies. In practice, a few terms are required ($N = 10$ is a usual value). Furthermore, in the right hand side of (20), the new kernels $\exp(-\omega_k(t-\tau))$ can now be expanded in Taylor series, which removes the need of storing all the signal history.

This Taylor development relies on the following time derivative identity:

$$\partial_t \int_0^t \exp(-\omega_k(t-\tau)) f(\tau) d\tau = f(t) - \omega_k \int_0^t \exp(-\omega_k(t-\tau)) f(\tau) d\tau \quad (21)$$

According to (20), with the following notation:

$$c_k(t) = C \int_0^t \exp(-\omega_k(t-\tau)) f(\tau) d\tau \quad (22)$$

it comes:

$$c(t) \cong C A_0 f(t) + \sum_{k=1}^N A_k \omega_k c_k(t) \quad (23)$$

Now, using (21) with a time increment δt , we can consider:

$$c_k(t) \cong C \delta t f(t) + (1 - \omega_k \delta t) c_k(t - \delta t) \quad (24)$$

so that, the computation of $c(t)$ relies only on the value of $f(t)$ and $c_k(t - \delta t)$ (with initial values $c_k(0) = 0$).

Quantities N , A_k and ω_k are carefully chosen, in order to get an efficient and accurate approximation of $c(t)$. For that purpose, a high and low cutoff frequencies, respectively ω_h and ω_l , are introduced. Then, N is the first integer greater than

$\frac{3}{2} \log_{10} \left(\frac{\omega_h}{\omega_l} \right)$. In practice, $\omega_h = \frac{1}{\delta t_{\max}}$ and $\omega_l = \frac{2\pi}{1000 t_{\text{end}}}$, where δt_{\max} is the greatest simulation time increment and t_{end}

is the final simulation time step. In fact, ω_h is enforced to be δt_{\max}^{-1} , to ensure the convergence of approximation (24). For instance, with $t_{\text{end}} = 100 \mu\text{s}$ and $\delta t_{\max} = 10 \text{ ns}$, it comes $\omega_h = 100 \text{ MHz}$, while $\omega_l = 62.8 \text{ Hz}$ and $N = 10$.

Amplitudes A_k and frequencies ω_k are introduced while establishing (20). Indeed, with H denoting the Heaviside step function, the quantity $c(t)$ can be rewritten as:

$$c(t) = \int_0^{+\infty} (t-\tau)^{-n} H(t-\tau) f(\tau) d\tau \quad (25)$$

and denoting the Laplace transform by L , we use the following identity:

$$\begin{aligned} (t-\tau)^{-n} H(t-\tau) &= L^{-1}\left(L(\tau^{-n} H(\tau), \omega), t-\tau\right) \\ &= L^{-1}(\Gamma(1-n) \omega^{n-1}, t-\tau) \end{aligned} \quad (26)$$

where Γ is the classical Gamma function.

The Prony series is introduced by considering the following approximation:

$$\omega^{n-1} \cong C_0 \prod_{k=1}^N \frac{1 + \frac{\omega}{\omega_k}}{1 + \frac{\omega}{\omega_k}} \quad (27)$$

where C_0 is a constant to be determined and the N principal frequencies are computed recursively by:

$$\omega_k = \left(\frac{\omega_h}{\omega_l}\right)^{\frac{1}{N}} \omega_{k-1} \quad \text{with} \quad \omega_1 = \left(\frac{\omega_h}{\omega_l}\right)^{\frac{n}{2N}} \omega_l \quad (28)$$

and the auxiliary frequencies are given by $\omega'_k = \left(\frac{\omega_h}{\omega_l}\right)^{\frac{1-n}{N}} \omega_k$.

After a partial fraction expansion, it comes:

$$\prod_{k=1}^N \frac{1 + \frac{\omega}{\omega_k}}{1 + \frac{\omega}{\omega_k}} = A_0 + \sum_{k=1}^N \frac{A_k}{1 + \frac{\omega}{\omega_k}} \quad (29)$$

where the N corresponding amplitudes are:

$$A_k = \prod_{j=1}^N \left(1 - \frac{\omega_k}{\omega_j}\right) \prod_{j=1, j \neq k}^N \left(1 - \frac{\omega_k}{\omega_j}\right)^{-1} \quad (30)$$

the initial one being $A_0 = 1 - \sum_{k=1}^N A_k$.

So, we obtain the following approximation:

$$(t-\tau)^{-n} H(t-\tau) \cong L^{-1}\left(C A_0 + \sum_{k=1}^N \frac{C A_k}{1 + \frac{\omega}{\omega_k}}, t-\tau\right) \cong C A_0 \delta(t-\tau) + \sum_{k=1}^N C A_k \omega_k \exp(-\omega_k (t-\tau)) \quad (31)$$

where δ is the Dirac function.

Finally, the remaining constant $C = \Gamma(1-n) C_0$ is determined such that for a constant signal $f(\tau) = 1$, a perfect equality between $(t-\tau)^{-n}$ and its approximation is attained at a specific time $(t-\tau) = \bar{t}$. Considering the mean time $\bar{t} = (\omega_h \omega_l)^{-1/2}$, it comes:

$$C = \frac{\bar{t}^{-n}}{\sum_{k=1}^N A_k \omega_k \exp(-\omega_k \bar{t})} \quad (32)$$

Appendix 2: HMX ignition and exponent computation

The exponent n , appearing in the ignition criterion building (section 3.1), has to be determined by fitting a power law relationship between the ignition time t_{ig} and a constant flux $\bar{\varphi}$, imposed on a micro-surface of constant radius \bar{R}_c . Following the work of Browning and Scammon [8], we establish this relationship by considering the global multistep chemical kinetic model for the thermal decomposition of HMX, proposed by Tarver [20] and [21]. The experimental data for the Tarver model in [17] involves laser induced ignition of HMX, with ignition time from 80 milliseconds to 2 seconds. Obviously, there is a 10^3 factor between this lowest ignition time and our ignition timing. However, in the work of [22], measurements have been made about ignition times from 2 nanoseconds to 30 000 seconds. It is shown in [22] that the Tarver decomposition model interpolates well the ignition times between 2 nanoseconds and 300 micro-seconds, which is in agreement with our observed ignition timing.

This model relies on four reactions and five chemical species. The reaction sequence is:



Each reaction source term \dot{q}_A , \dot{q}_B , \dot{q}_C and \dot{q}_D is based on an Arrhenius kinetic law:

$$\dot{q}_I = \alpha^{m_I} Q_I Z_I \exp\left(-\frac{E_I}{R T}\right) \quad (33)$$

where $I = A, B, C$ or D , α is the mass fraction of the left hand side specie, m_I the reaction order, Q_I the heat of reaction per unit of volume, Z_I the frequency factor, E_I the activation energy, R the gas constant and T the temperature. The chemical kinetic parameters for the HMX (coarse grains) decomposition model are listed in Table 4, according to [21].

Table 4. parameters of HMX decomposition.

reaction	reaction order m_I	heat of reaction Q_I (MJ.m ⁻³)	$\ln \frac{Z_I}{1 \text{ s}^{-1}}$	activation energy E_I (kJ.mol ⁻¹)
A	1	-76	48.1	203
B	1	-460	48.7	220
C	1	1 000	37.8	185
D	2	10 000	28.1	143

Mass fractions of β -HMX (α_A), δ -HMX (α_B), intermediate solid (α_C), intermediate gas (α_D) and final gas (α_E) are computed by a 4-th order explicit Runge-Kutta scheme for the following conservation laws:

$$\begin{cases} \dot{\alpha}_A = -\alpha_A Z_A \exp\left(-\frac{E_A}{R T}\right) \\ \dot{\alpha}_B = \alpha_A Z_A \exp\left(-\frac{E_A}{R T}\right) - \alpha_B Z_B \exp\left(-\frac{E_B}{R T}\right) \\ \dot{\alpha}_C = \alpha_B Z_B \exp\left(-\frac{E_B}{R T}\right) - \alpha_C Z_C \exp\left(-\frac{E_C}{R T}\right) \\ \dot{\alpha}_D = \alpha_C Z_C \exp\left(-\frac{E_C}{R T}\right) - \alpha_D^2 Z_D \exp\left(-\frac{E_D}{R T}\right) \\ \dot{\alpha}_E = \alpha_D^2 Z_D \exp\left(-\frac{E_D}{R T}\right) \end{cases} \quad (34)$$

Furthermore, the mass conservation equation for the chemical species is satisfied:

$$\alpha_A + \alpha_B + \alpha_C + \alpha_D + \alpha_E = 1 \quad (35)$$

Temperature T is computed by solving the heat flux equation with Abaqus/Standard (convection and diffusion):

$$\rho C_p \dot{T} - \lambda \Delta T = \dot{q}_A + \dot{q}_B + \dot{q}_C + \dot{q}_D \quad (36)$$

where ρ is the HMX density, C_p the HMX specific heat and λ the HMX conductivity. In fact, this conductivity is low (0.4 W/m/K) and it takes several milliseconds for the heat to really diffuse out.

In preliminary studies, such a thermal decomposition model has been used to compute, with a good accuracy, times-to-explosion for PBX confined in an ODTX apparatus (One Dimension Time to eXplosion [21]). For sufficiently high initial temperatures at the PBX boundary, these explosion times correspond to a very high rising of the temperature, which leads to a value for the source term $\dot{q}_A + \dot{q}_B + \dot{q}_C + \dot{q}_D$ greater than $180 \text{ MW}\cdot\text{m}^{-3}$. Therefore, in our computations, the ignition time t_{ig} is the timestamp at which equality is reached between the source term and the threshold value of $180 \text{ MW}\cdot\text{m}^{-3}$.

Contrary to [8], this thermal decomposition model is now applied at the grain scale, as illustrated in Figure 21. Axisymmetrical computations are performed with a HMX grain of $200 \mu\text{m}$ (diameter) and four different contact surface radii \bar{R}_c : 12.5, 25, 50 and $100 \mu\text{m}$. Thanks to symmetry reasons, only half of the upper grain section is represented (Figure 21).

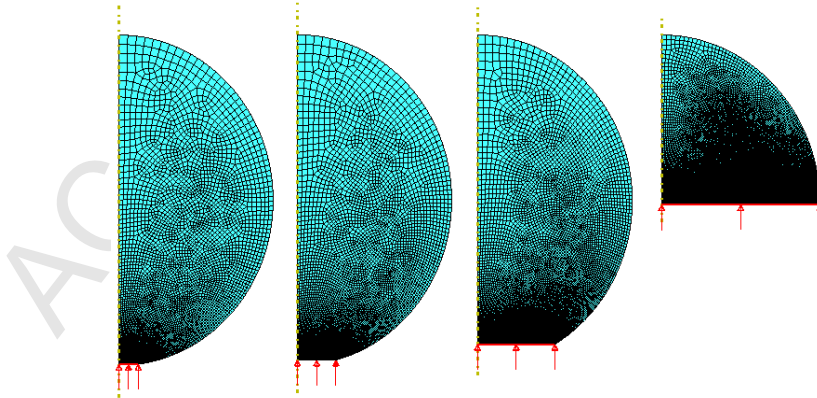


Fig. 21. Different HMX grains with an imposed heat flux on a surface with a radius of, respectively, 12.5, 25, 50 and $100 \mu\text{m}$ (a mesh size of 250 nm is required on those surfaces, other surfaces being considered as adiabatic).

Various constant heat fluxes $\bar{\varphi}$ are imposed on the contact surface: 10^7 , 10^8 and 10^9 W.m⁻². According to equation (11), with a constant a_4 of 77.7 m.Pa^{2/3} for HMX, a flux of 10^7 W.m⁻² corresponds, for instance, to a 0.1 MPa pressure and a 2 780 s⁻¹ plastic shear rate, while 10^9 W.m⁻² corresponds to a 500 MPa pressure and a 16 250 s⁻¹ plastic shear rate.

According to [8], we study the evolution of fluence $\bar{\varphi} t_{ig}$ against ignition time t_{ig} , with different radii \bar{R}_c . In practice, this evolution is investigated after an appropriate scaling: $\pi_1 = \frac{C_p}{Q \lambda} \bar{\varphi} \bar{R}_c$ is the scaled flux and $\pi_2 = \frac{\lambda}{\rho C_p} \frac{t_{ig}}{\bar{R}_c^2}$ is the scaled time, Q being a global reaction energy per unit of volume. So as to compute a power law interpolation, a log-log graph is plotted between the scaled fluence $\pi_1 \pi_2$ and the scaled time π_2 (Figure 22).

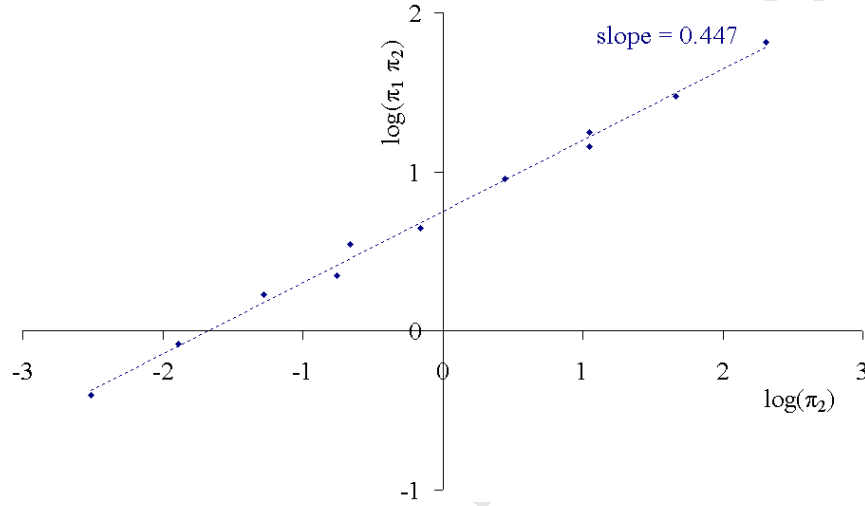


Fig. 22. The log of scaled fluence is quite well linear with the log of scaled time: a power law interpolation is relevant.

From a linear fitting, it comes:

$$\pi_1 \pi_2 = a_8 \pi_2^n \quad (37)$$

where a_8 is a dimensionless constant and exponent n is 0.447. This power law can be expressed as follows:

$$\bar{\varphi} \bar{R}_c = \frac{Q \lambda^n}{\rho^{n-1} C_p^n} a_8 \left(\frac{t_{ig}}{\bar{R}_c^2} \right)^{n-1} \quad (38)$$

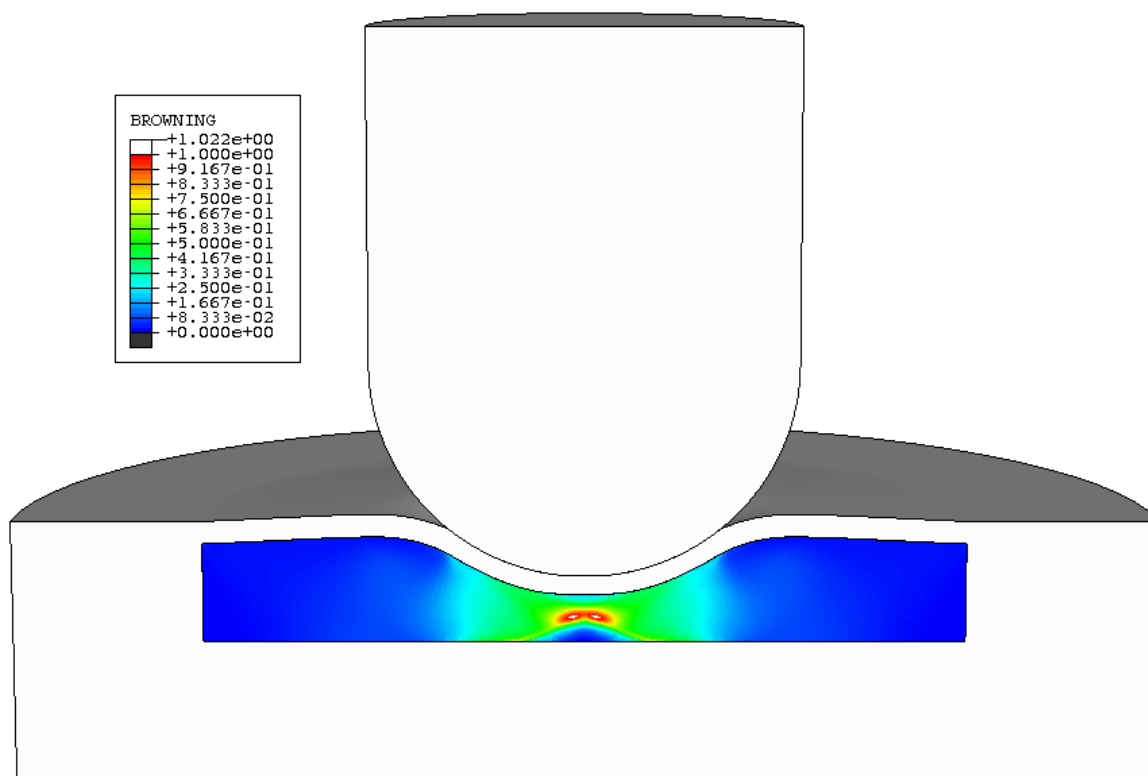
which gives equation (14) with $a_5 = \frac{Q \lambda^n}{\rho^{n-1} C_p^n} a_8$.

Acknowledgments

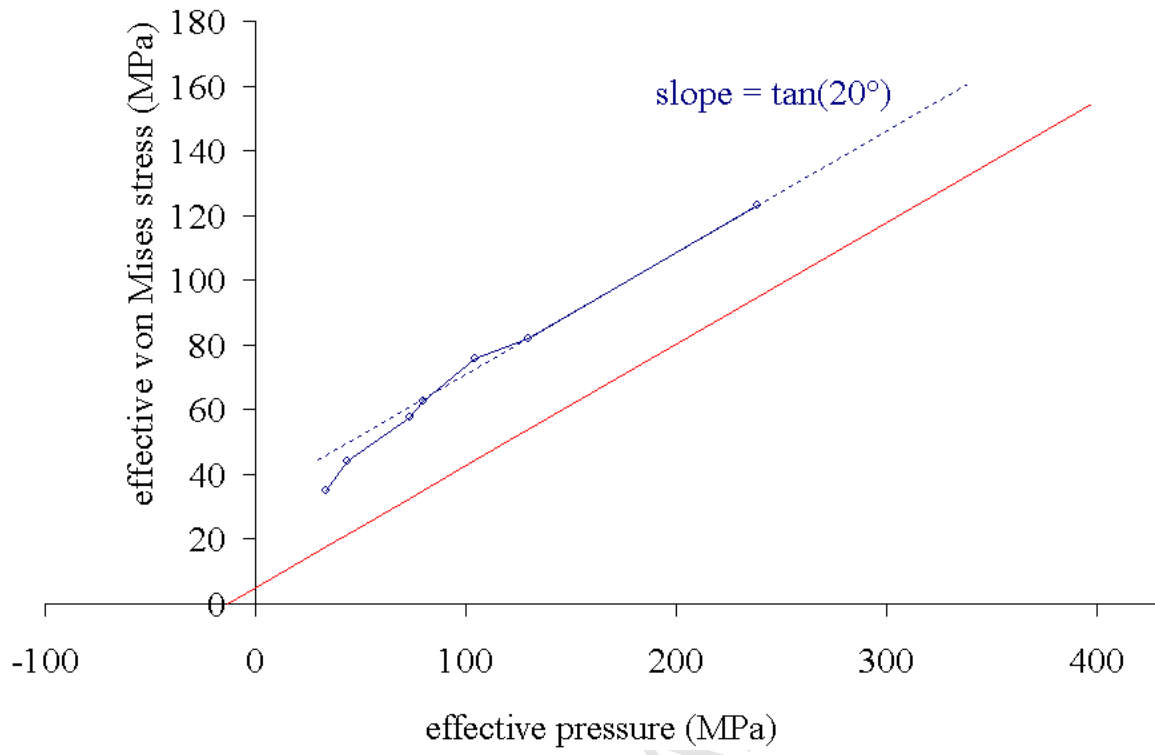
Authors wish to thank gratefully M. Biessy, E. Espinet, C. Calteau and other contributors from the reactive experiment facility team, J. Belair, M. Leblanc and S. Veyre for their work on Abaqus, J.-L. Brigolle, P. Lambert, M. Labrunie, Y. Sadou and P. Rey for their work on PBX. Reviewer's helpful suggestions are also deeply acknowledged.

References

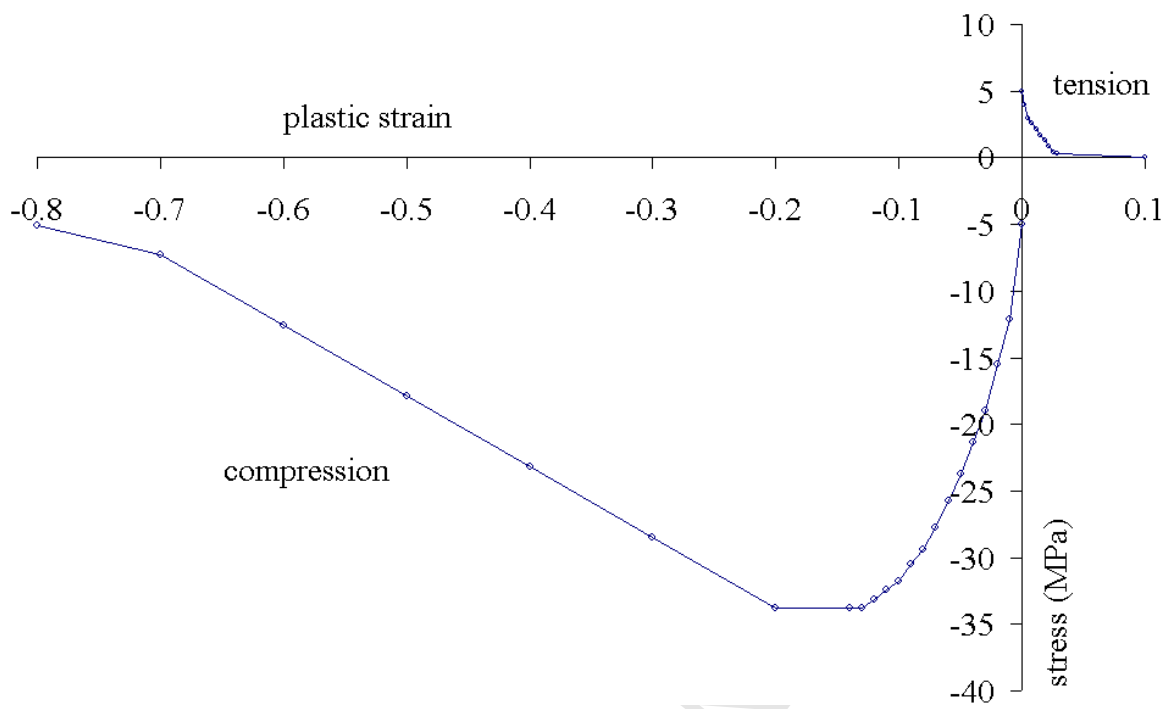
- [1] Chidester, Green, Lee, A frictional work predictive method for the initiation of solid high explosives from low-pressure impacts, Proc. 10th International Detonation Symposium, Boston, 1993.
- [2] Delmaire-Sizes, Belmas, Picart, Trumel, Low-velocity impact tests on an HMX-based explosive, Proc. 34th International Pyrotechnics Seminar, Beaune, 2007.
- [3] Field, Bourne, Plamer, Walley, Hot-spot ignition mechanisms for explosives and propellants, Philosophical Transaction of the Royal Society of London A 339 (1992) 269-283.
- [4] Dienes, Frictional hot-spots and propellant sensitivity, Proc. Material Research Society Symposium 24 (1984) 373-381.
- [5] Partom, A threshold criterion for impact ignition, Proc. 12th International Detonation Symposium, San Diego, 2002.
- [6] Browning, Microstructural model of mechanical initiation of energetic materials, Proc. Shock Waves in Condensed Matter, Amsterdam, 1995.
- [7] Scammon, Browning, Middelich, Dienes, Haberman, Bennett, Low amplitude insult project: structural analysis and prediction of low order reaction, Proc. 11th International Detonation Symposium, Snowmass, 1998.
- [8] Browning, Scammon, Microstructural model of ignition for time varying loading conditions, Proc. Shock Waves in Condensed Matter, Saint Petersburg, 2001.
- [9] Chidester, Tarver, Garza, Low amplitude impact testing and analysis of pristine and aged solid high explosives, Proc. 11th International Detonation Symposium, Snowmass, 1998.
- [10] Dienes, A unified theory of flow, hot spots, and fragmentation with application to explosive sensitivity, in High-Pressure Shock Compression of Solids II, Springer-Verlag New York, Lee Davison et al., eds.
- [11] Vandersall, Chidester, Forbes, Garcia, Greenwood, Switzer, Tarver, Experimental and modeling studies of crush, puncture, and perforation scenarios in the Steven impact test, Proc. 12th International Detonation Symposium, San Diego, 2002.
- [12] Vandersall, Murty, Chidester, Forbes, Garcia, Greenwood, Tarver, Investigation of Steven impact test using a transportation hook projectile with gauged experiments and 3D modeling, Proc. Compression Waves in Condensed Matter, Portland, 2003.
- [13] Bazant, Adley, Carol, Jirasek, Akers, Rohani, Cargile, Caner, Large-strain generalization of microplane model for concrete and application, Journal of Engineering Mechanics 126 (2000) 971-980.
- [14] Grange, Mencacci, Hild, Modelling dynamic fragmentation of rocks, Journal of Physics IV France 134 (2006) 125-131.
- [15] Espinosa, Dwivedi, Zavattieri, Yuan, A numerical investigation of penetration in multilayered material/structure systems, International Journal of Solids and Structures 35 (1998) 2975-3001.
- [16] Gruau, Picart, Bianchi, Perlat, Verbeek, Sholtes, Simulation of PBX when submitted to low velocity mechanical impacts, Proc. 17th Dymat Technical Meeting, Cambridge, 2007.
- [17] Lubliner, Oliver, Oller, Oñate, A plastic-damage model for concrete, International Journal of Solids and Structures 25-3 (1989) 299-326.
- [18] Lee, Fenves, Plastic-damage model for cyclic loading of concrete structures, Journal of Engineering Structures 124-8 (1998) 892-900.
- [19] Dey, Johnson, Shear band formation in plastic bounded explosives (PBX), Proc. Shock Compression of Condensed Matter, Amherst, 1997.
- [20] Tarver, Chemical kinetic modeling of HMX and TATB laser ignition tests, Energetic Materials 22 (2004) 93-107.
- [21] Tarver, Tran, Thermal decomposition models for HMX-based plastic bonded explosives, Combustion and Flame 137 (2004) 50-62.
- [22] Henson, Asay, Smilowitz, Dickson, Ignition chemistry in HMX from thermal explosion to detonation, Proc. Shock Compression of Condensed Matter, Atlanta, 2001.
- [23] Sabatier, Lanusse, Moze, Merveillaut, Trumel, Oustaloup, Past and some recent CRONE group applications of fractional differentiation - Part 2, Proc. Symposium on Applied Fractional Calculus, Badajoz, 2007.
- [24] Sabatier, Merveillaut, Oustaloup, Gruau, Trumel, Fractional integration for energetic material ignition prediction, Proc. Fractional Differentiation and its Applications, Ankara, 2008.
- [25] Gratton, Le, Frachon, Caliez, Picart, Mechanical behaviour of a viscoelastic plastic granular material: experimental procedure and modelling, WSEAS Transactions on Computers 5-1 (2006) 149-156.
- [26] Frachon, Caliez, Gratton, Le, Picart, Mechanical modelling and integration of a viscoelastic plastic material, sensitive to hydrostatic pressure – bend and brazilian tests calculations, Proc. 7th World Congress on Computational Mechanics, Los Angeles, 2006.
- [27] Vivier, Hild, Labrunie, Lambert, Trumel, Studying and modelling a pressed HMX-based energetic material, Proc. 17th Dymat Technical Meeting, Cambridge, 2007.
- [28] Vivier, Trumel, Hild, On the stored and dissipated energies in heterogeneous rate-independent systems, submitted to Cont. Mech. Thermodyn..



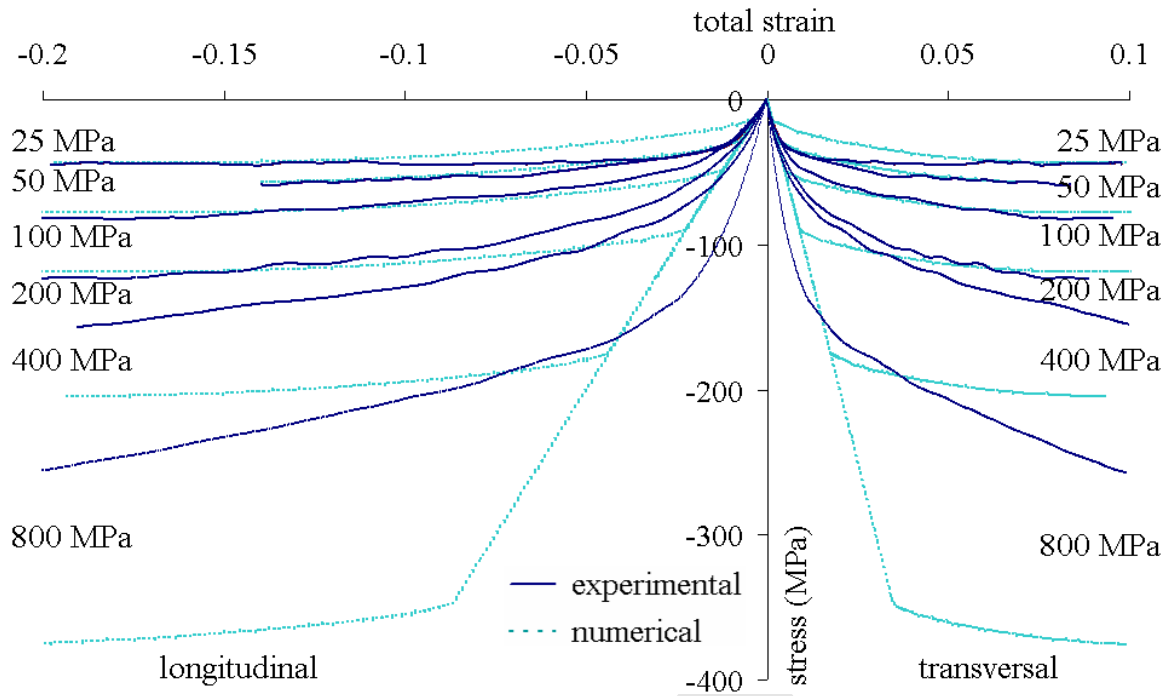
ACCEPTED MANUSCRIPT

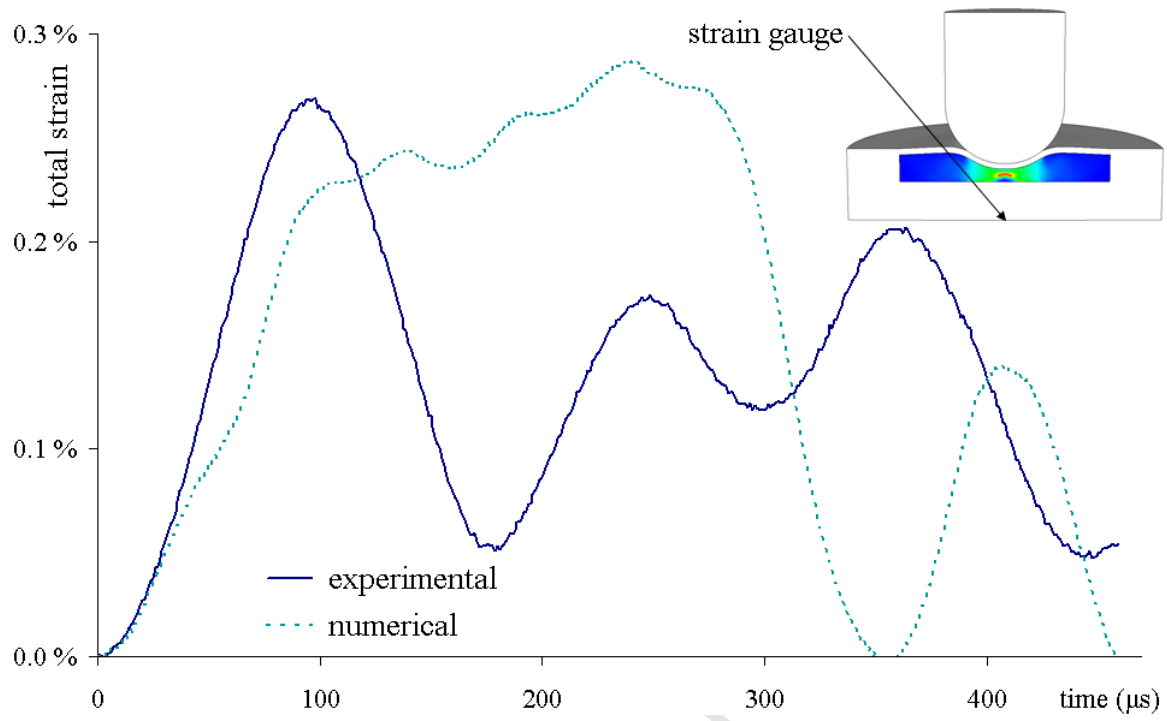


ACCEPTED MANUSCRIPT

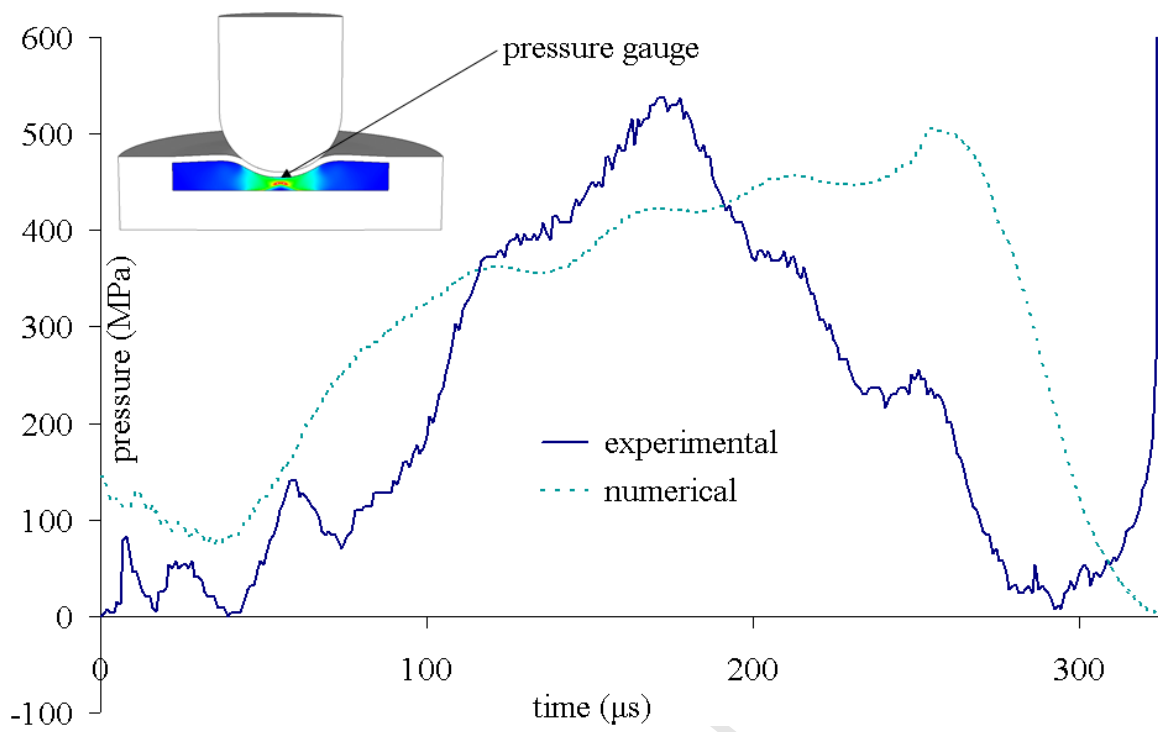


ACCEPTED MANUSCRIPT

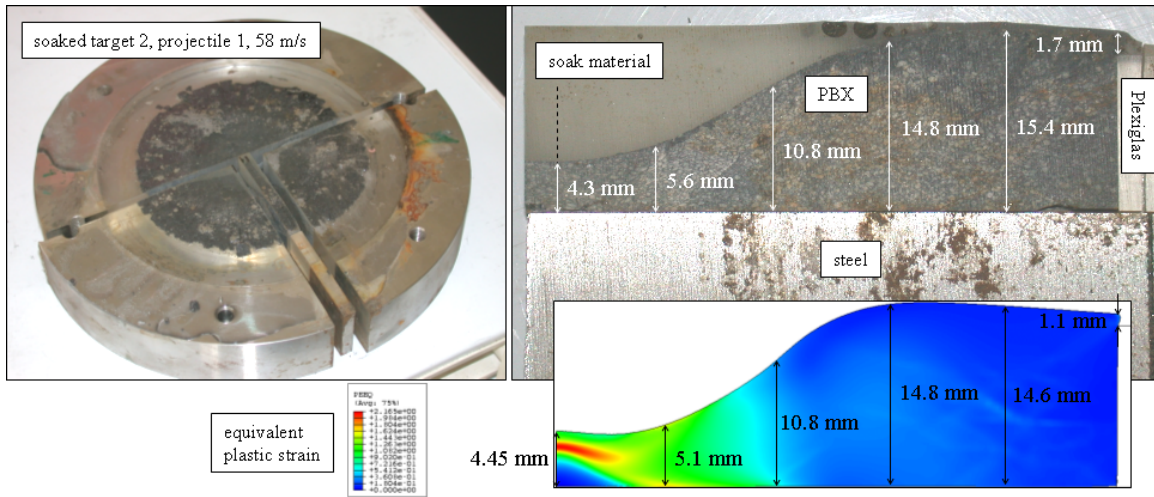


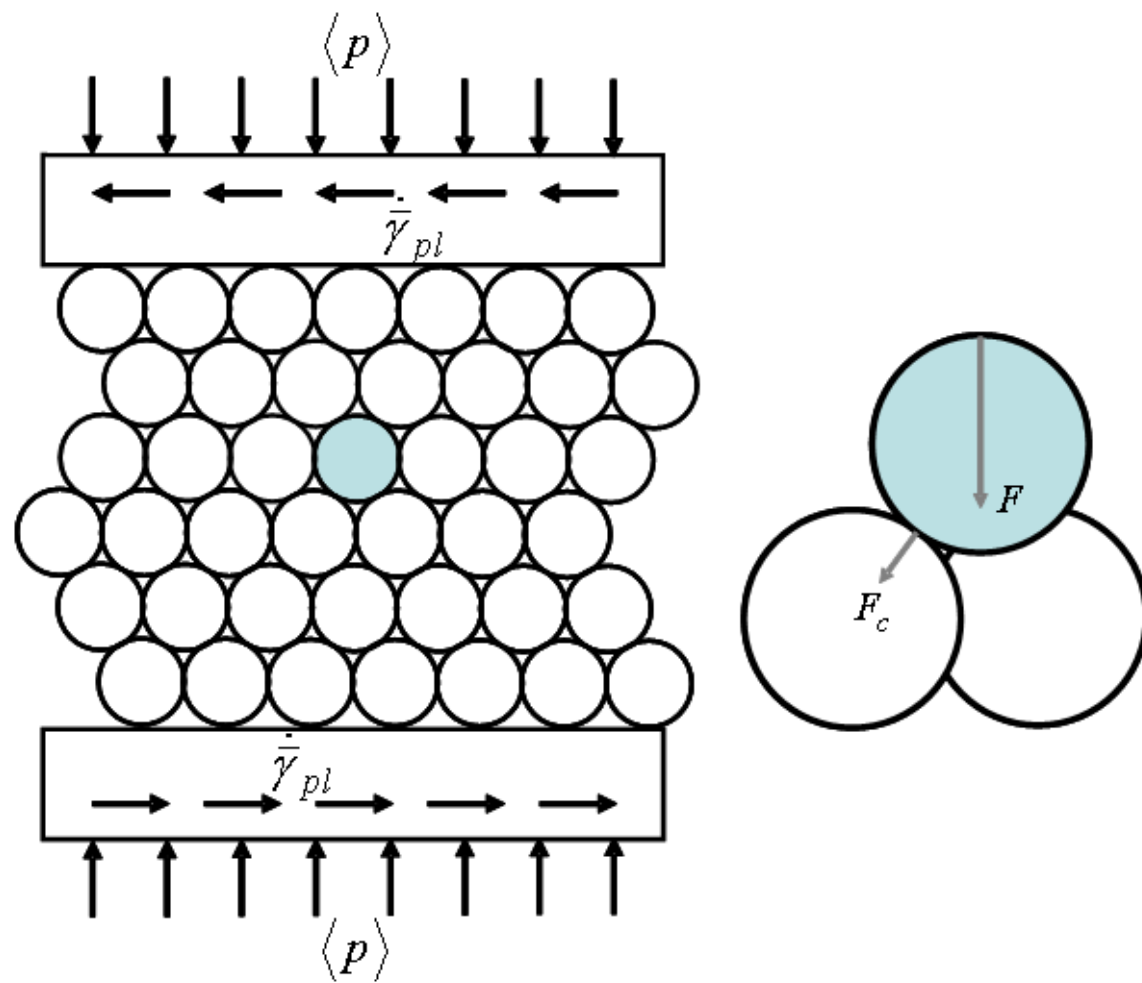


ACCEPTED MANUSCRIPT

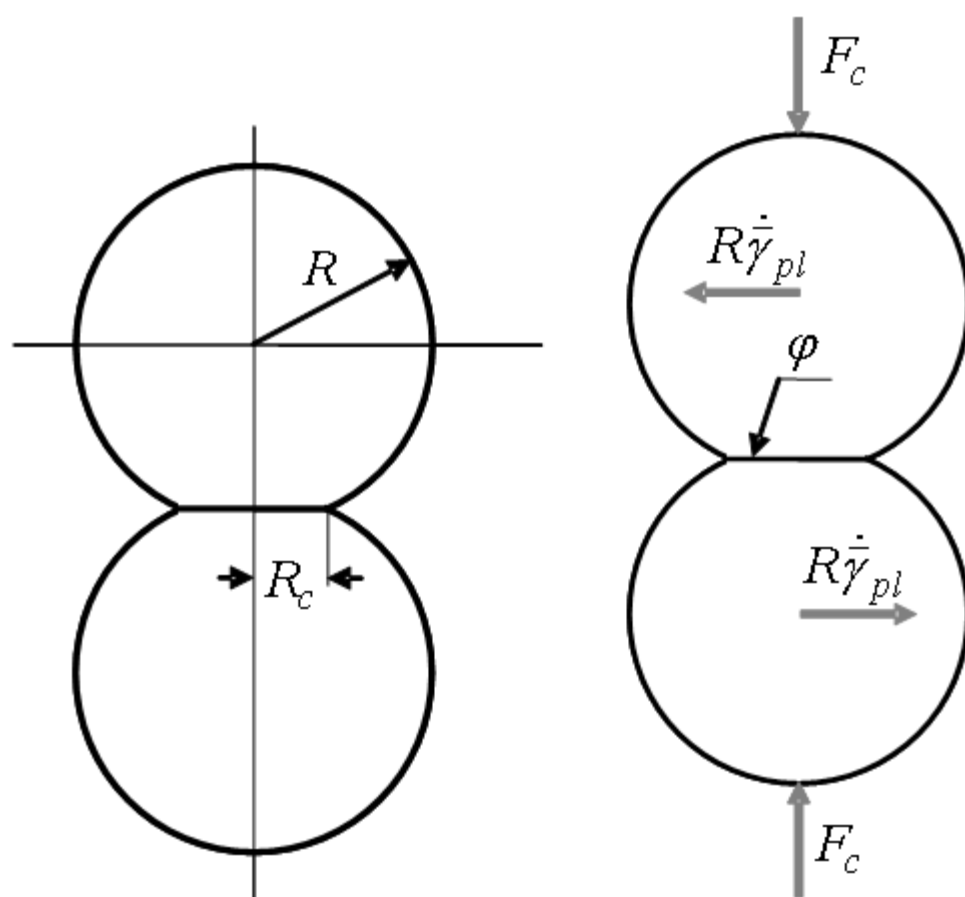


ACCEPTED MANUSCRIPT

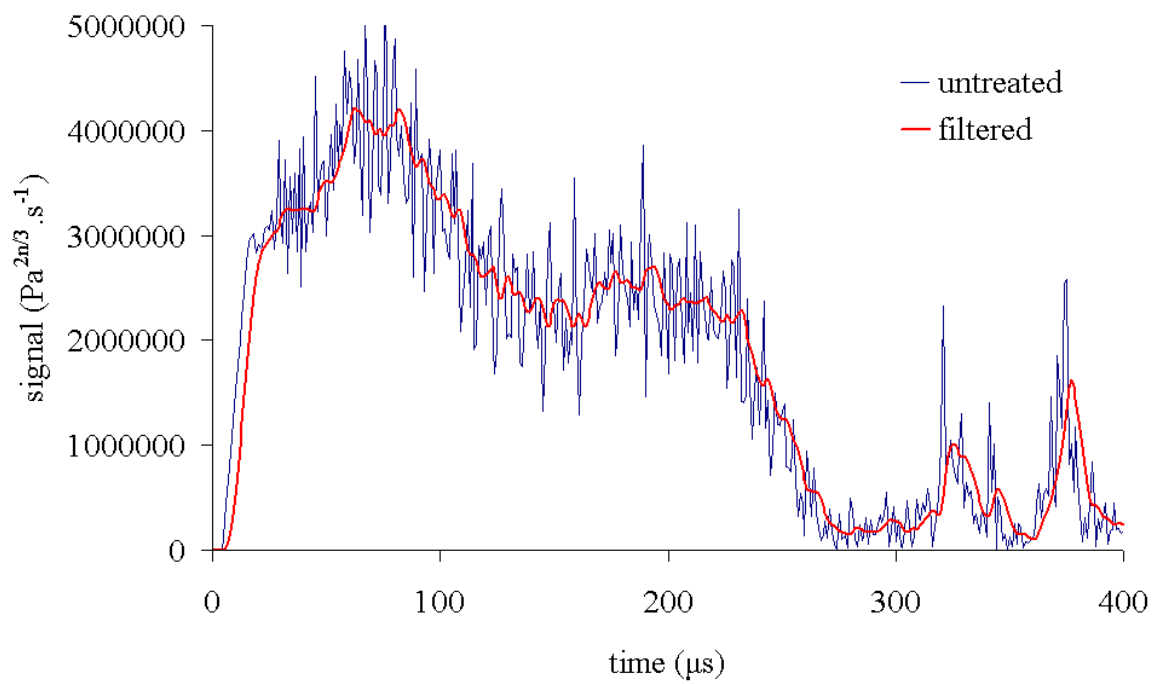




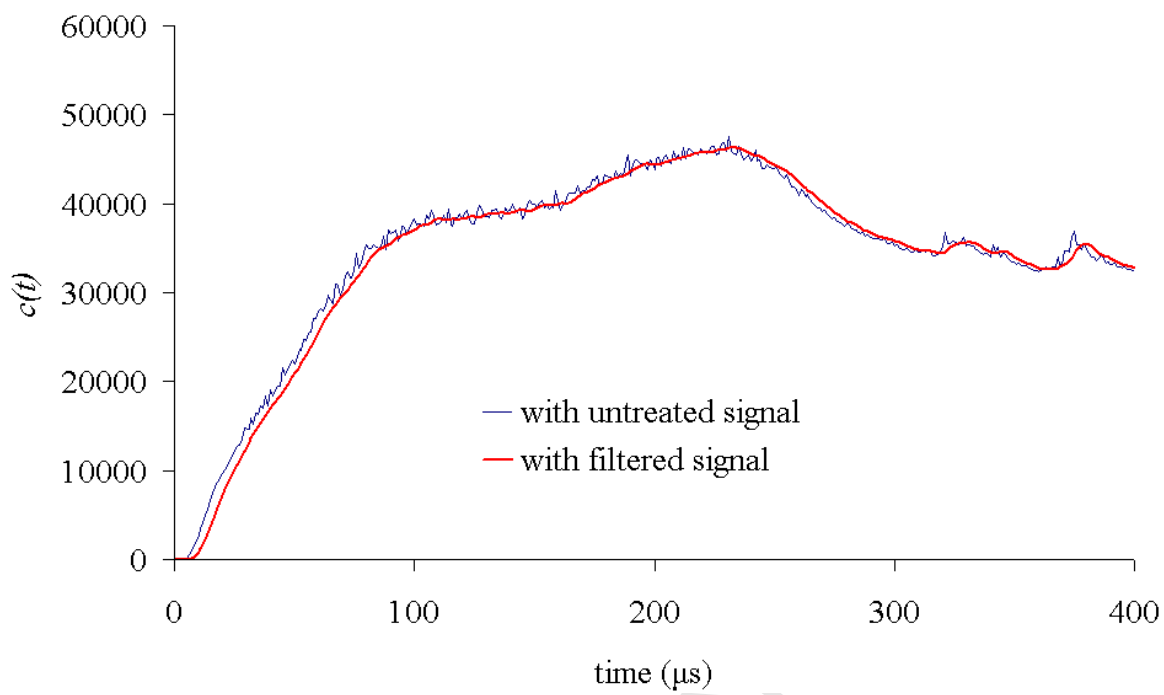
ACCEPTED



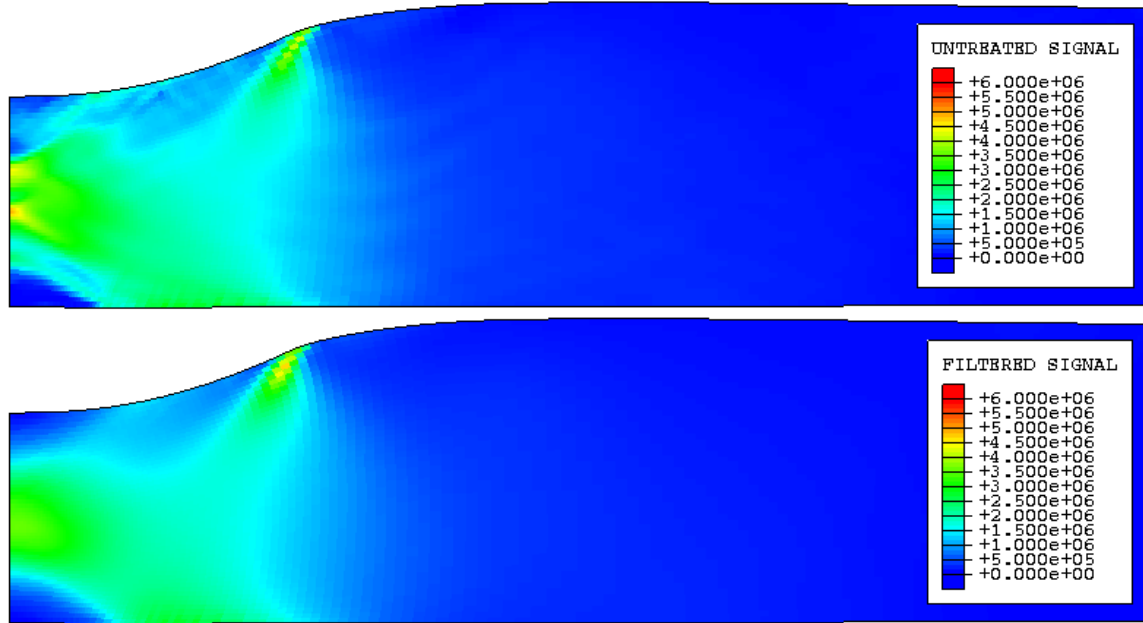
ACCEPTED

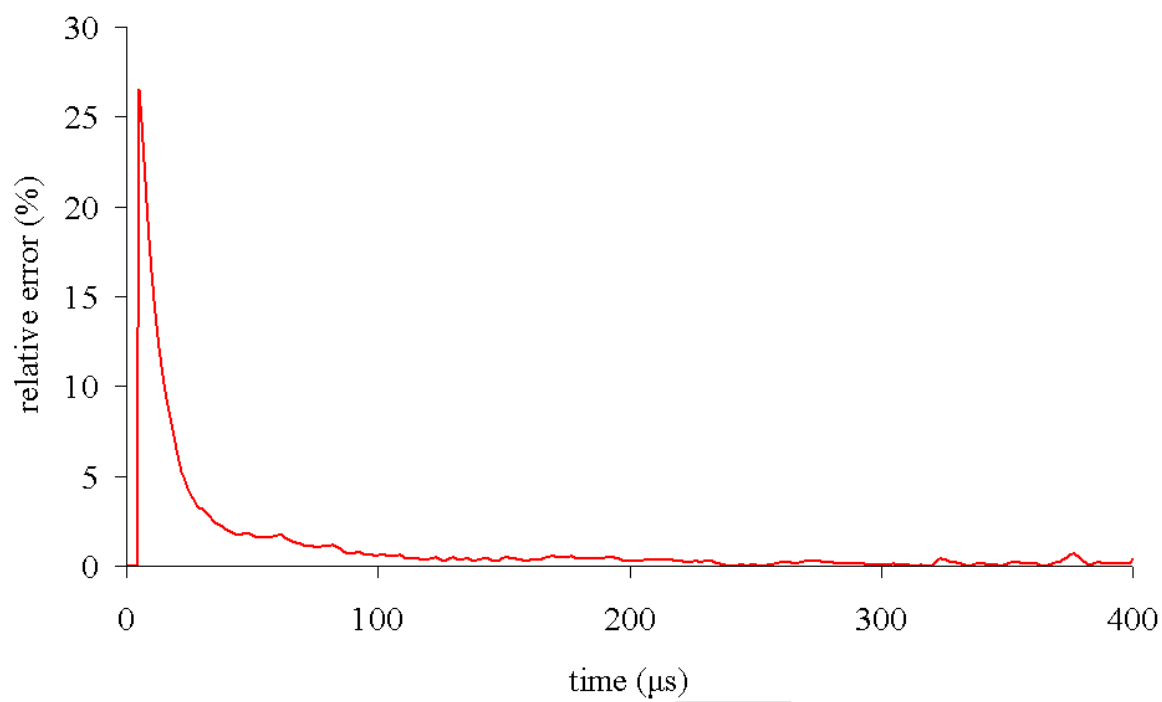


ACCEPTED MANUSCRIPT

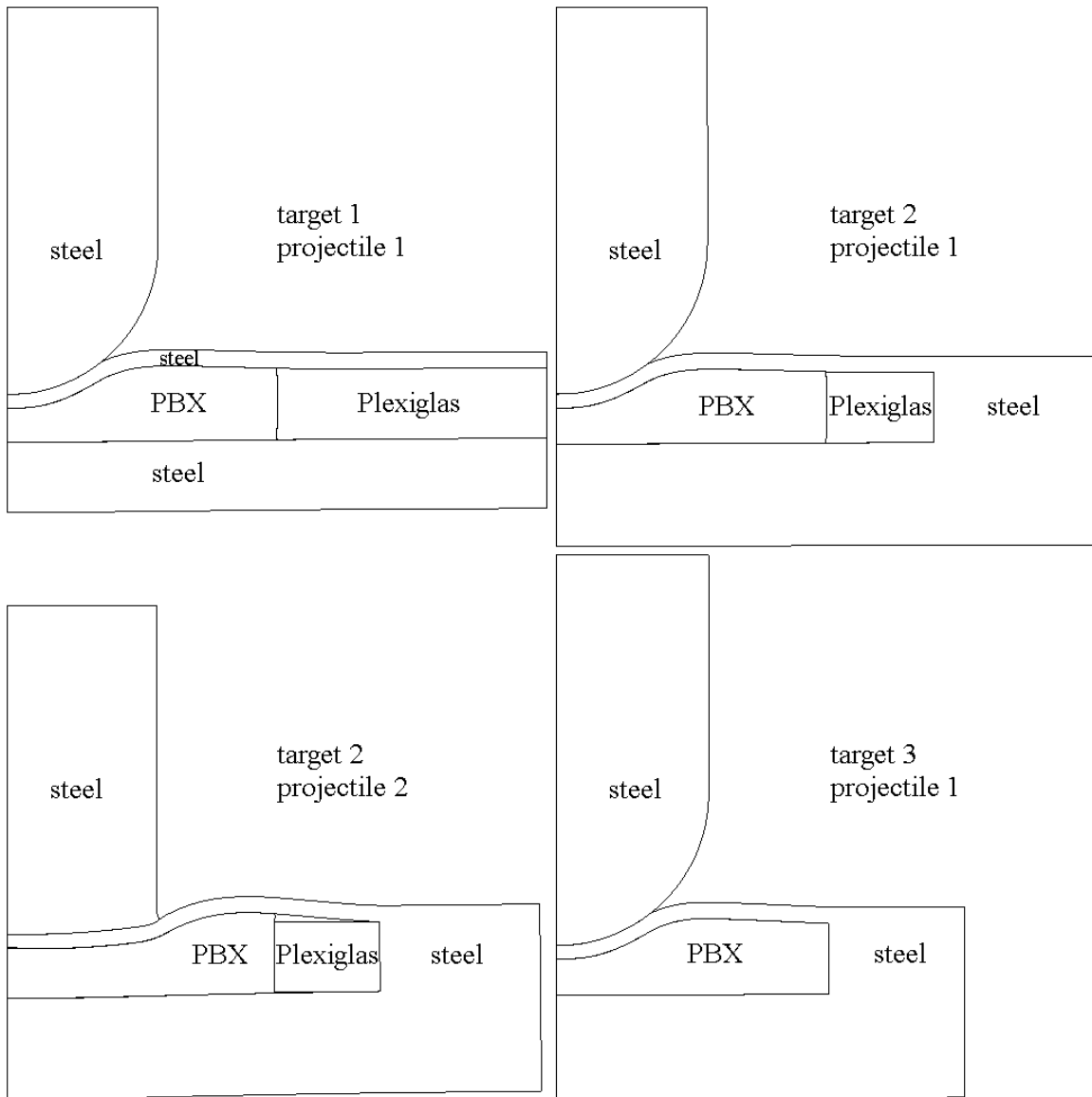


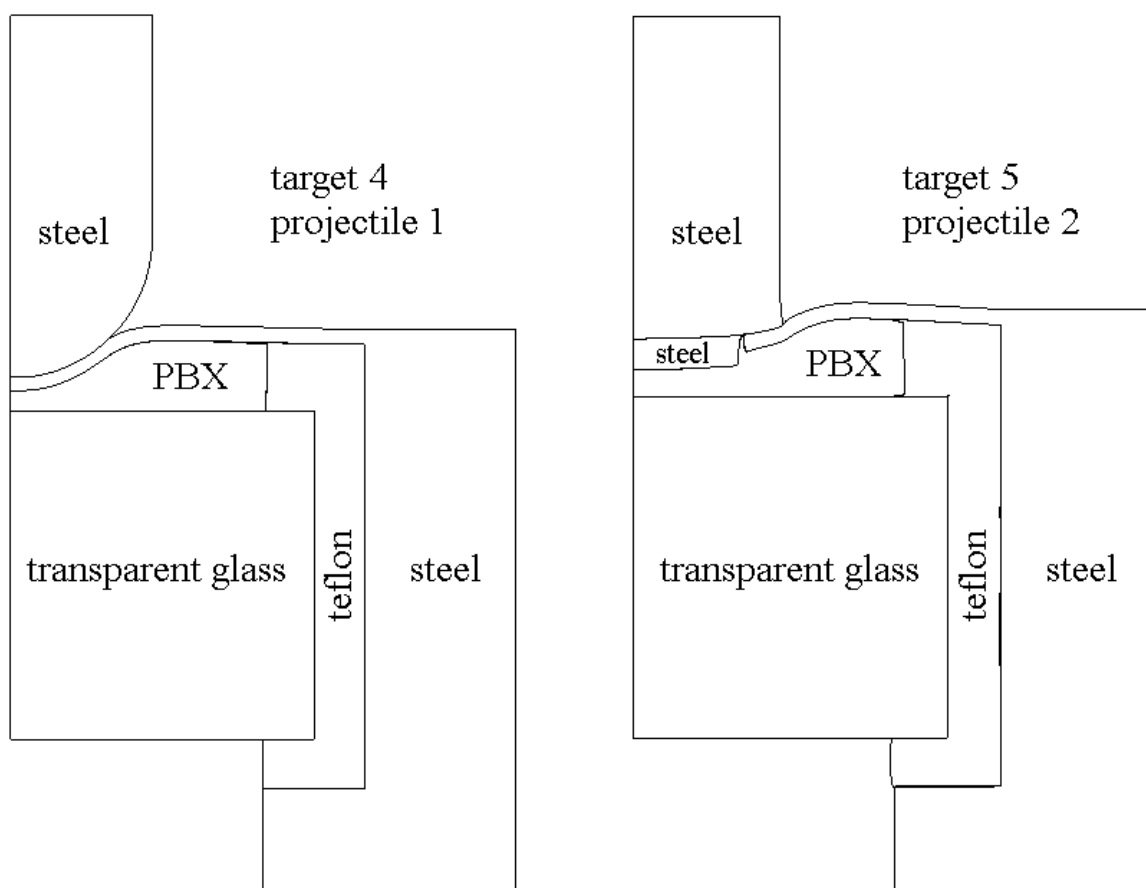
ACCEPTED MAN



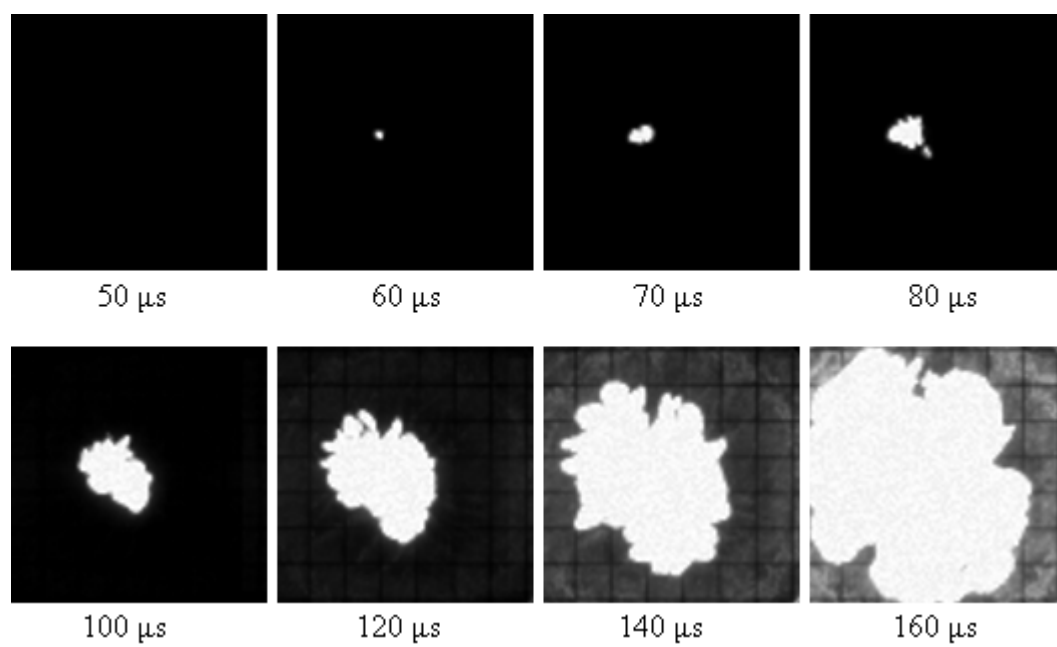


ACCEPTED MANUSCRIPT

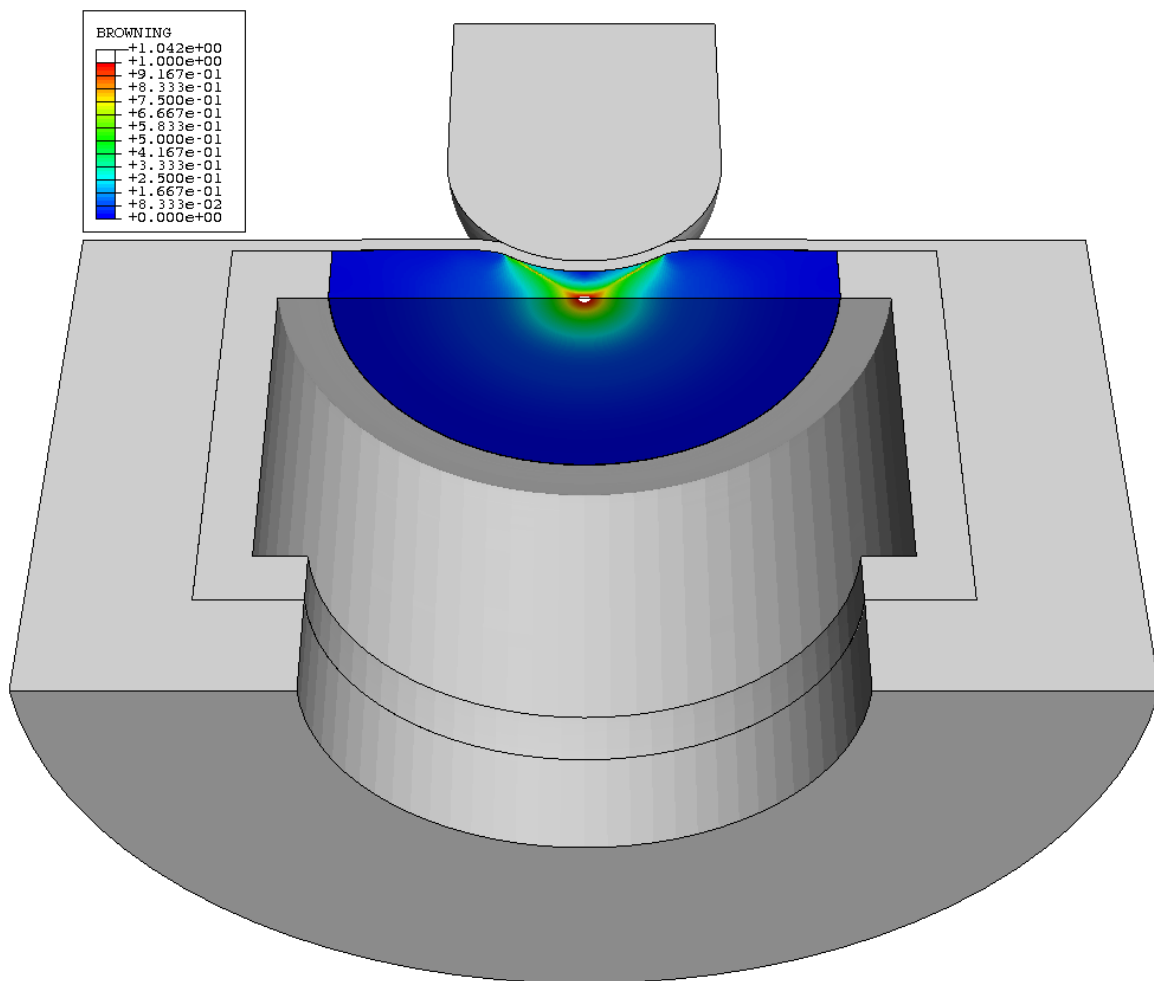




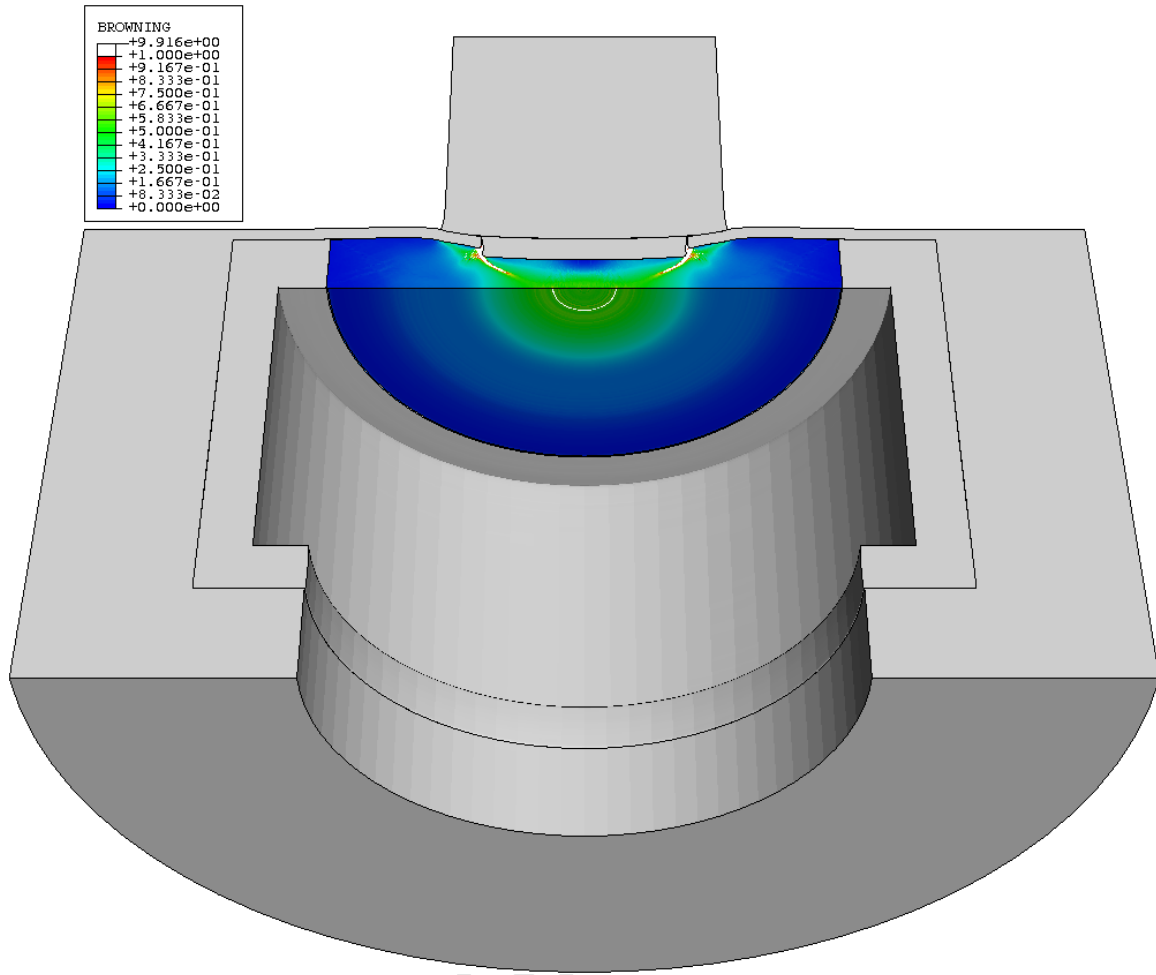
ACCEPTED

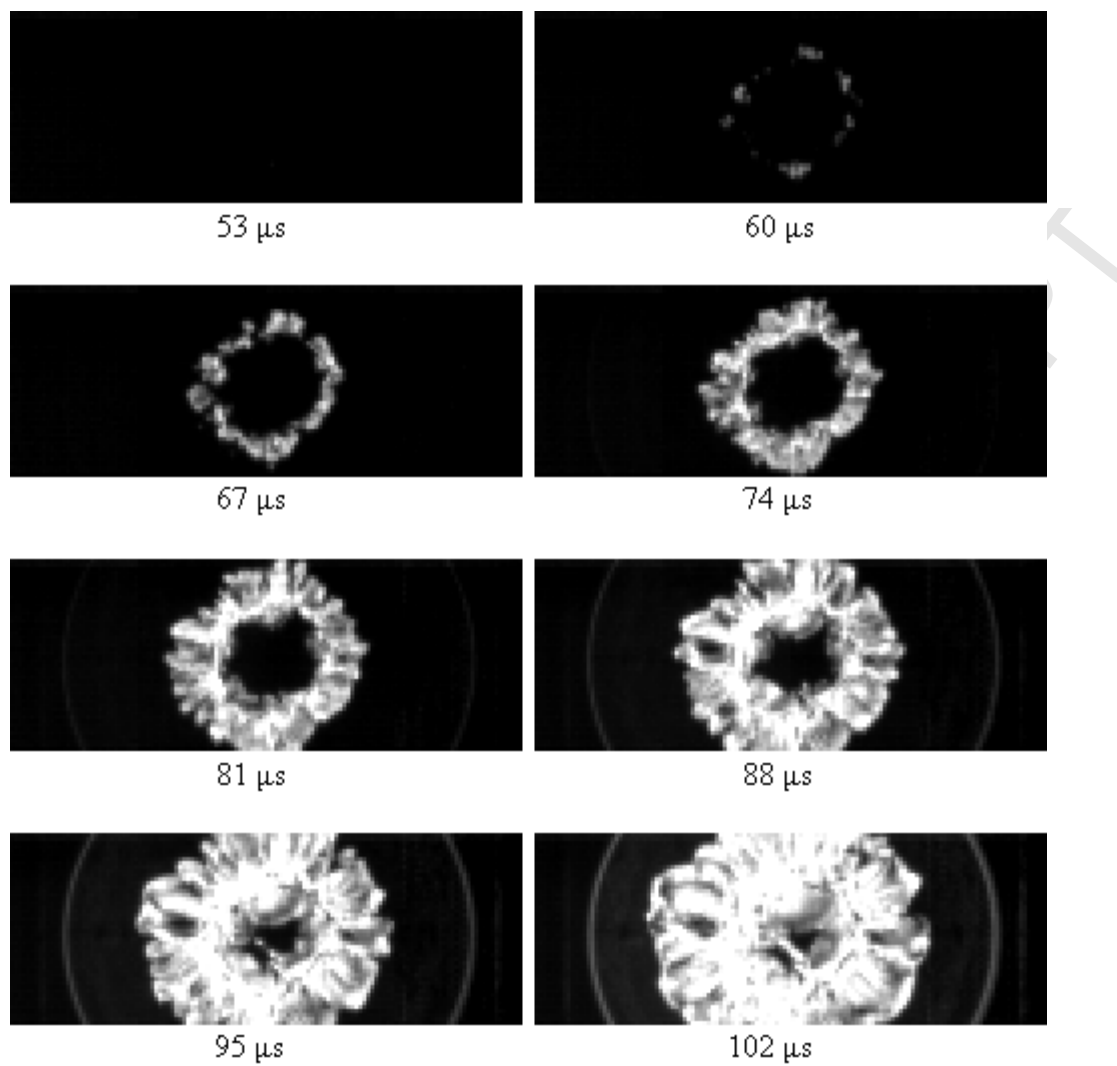


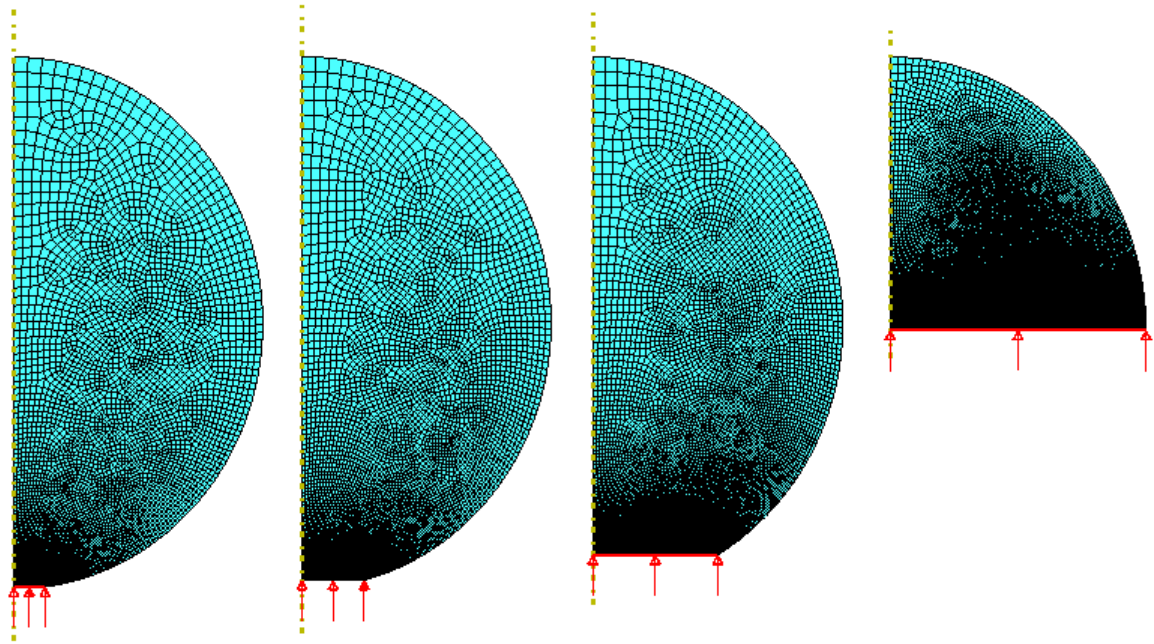
ACCEPTED MANUSCRIPT



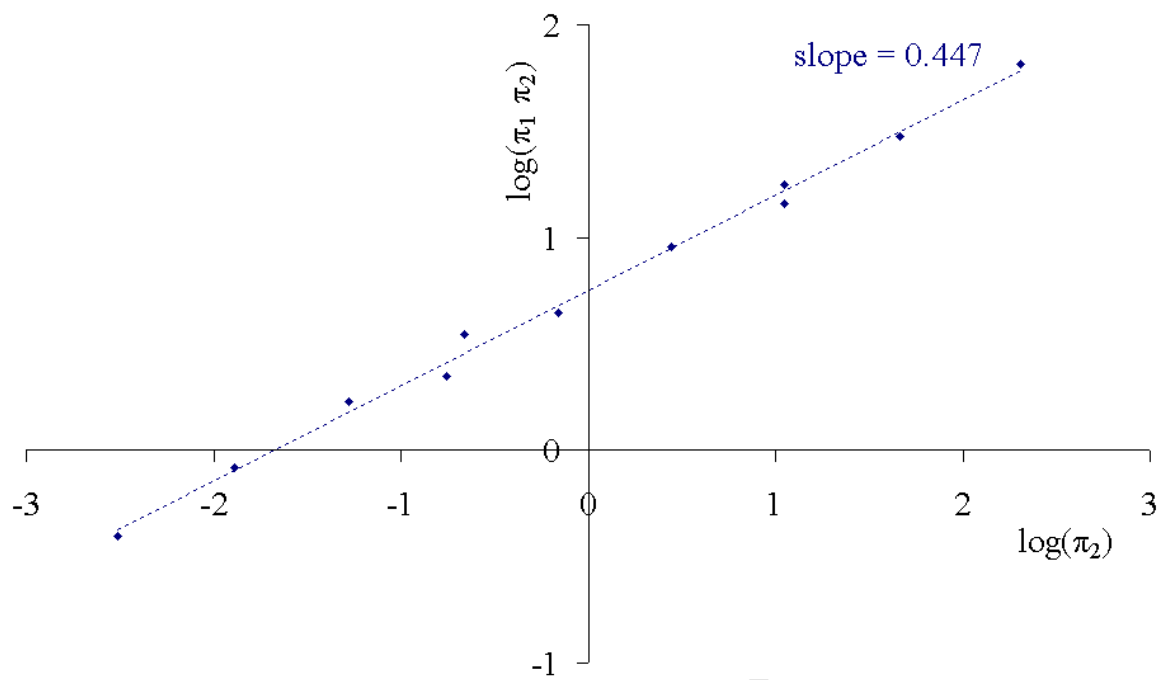
ACCEPTED







ACCEPTED MANUSCRIPT



ACCEPTED MAN